NOAA Technical Report NESDIS 140

Microburst Nowcasting Applications of GOES

Washington, D.C.
September 2011

U.S. DEPARTMENT OF COMMERCE
National Oceanic and Atmospheric Administration
National Environmental Satellite, Data, and Information Service

NOAA TECHNICAL REPORTS

National Environmental Satellite, Data, and Information Service

The National Environmental Satellite, Data, and Information Service (NESDIS) manages the Nation's civil Earth-observing satellite systems, as well as global national data bases for meteorology, oceanography, geophysics, and solar-terrestrial sciences. From these sources, it develops and disseminates environmental data and information products critical to the protection of life and property, national defense, the national economy, energy development and distribution, global food supplies, and the development of natural resources.

Publication in the NOAA Technical Report series does not preclude later publication in scientific journals in expanded or modified form. The NESDIS series of NOAA Technical Reports is a continuation of the former NESS and EDIS series of NOAA Technical Reports and the NESC and EDS series of Environmental Science Services Administration (ESSA) Technical Reports.

An electronic copy of this report may be obtained at:
http://www.star.nesdis.noaa.gov/star/smcd_pub.php

A limited number of copies of earlier reports are available by contacting Susan Devine, NOAA/NESDIS, E/RA, 5200 Auth Road, Room 701, Camp Springs, Maryland 20746, (301) 763-8127 x136. A partial listing of more recent reports appears below:

NESDIS 110 An Algorithm for Correction of Navigation Errors in AMSU-A Data. Seiichiro Kigawa and Michael P. Weinreb, December 2002.

NESDIS 111 An Algorithm for Correction of Lunar Contamination in AMSU-A Data. Seiichiro Kigawa and Tsan Mo, December 2002.

NESDIS 112 Sampling Errors of the Global Mean Sea Level Derived from Topex/Poseidon Altimetry. Chang-Kou Tai and Carl Wagner, December 2002.

NESDIS 113 Proceedings of the International GODAR Review Meeting: Abstracts. Sponsors: Intergovernmental Oceanographic Commission, U.S. National Oceanic and Atmospheric Administration, and the European Community, May 2003.

NESDIS 114 Satellite Rainfall Estimation Over South America: Evaluation of Two Major Events. Daniel A. Vila, Roderick A. Scofield, Robert J. Kuligowski, and J. Clay Davenport, May 2003.

NESDIS 115 Imager and Sounder Radiance and Product Validations for the GOES-12 Science Test. Donald W. Hillger, Timothy J. Schmit, and Jamie M. Daniels, September 2003.

NESDIS 116 Microwave Humidity Sounder Calibration Algorithm. Tsan Mo and Kenneth Jarva, October 2004.

NESDIS 117 Building Profile Plankton Databases for Climate and EcoSystem Research. Sydney Levitus, Satoshi Sato, Catherine Maillard, Nick Mikhailov, Pat Cadwell, Harry Dooley, June 2005.

NESDIS 118 Simultaneous Nadir Overpasses for NOAA-6 to NOAA-17 Satellites from 1980 and 2003 for the Intersatellite Calibration of Radiometers. Changyong Cao, Pubu Ciren, August 2005.

NESDIS 119 Calibration and Validation of NOAA 18 Instruments. Fuzhong Weng and Tsan Mo, December 2005.

NESDIS 120 The NOAA/NESDIS/ORA Windsat Calibration/Validation Collocation Database. Laurence Connor, February 2006.

NESDIS 121 Calibration of the Advanced Microwave Sounding Unit-A Radiometer for METOP-A. Tsan Mo, August 2006.

NESDIS 122 JCSDA Community Radiative Transfer Model (CRTM). Yong Han, Paul van Delst, Quanhua Liu, Fuzhong Weng, Banghua Yan, Russ Treadon, and John Derber, December 2005.

NESDIS 123 Comparing Two Sets of Noisy Measurements. Lawrence E. Flynn, April 2007.

NESDIS 124 Calibration of the Advanced Microwave Sounding Unit-A for NOAA-N'. Tsan Mo, September 2007.

NESDIS 125 The GOES-13 Science Test: Imager and Sounder Radiance and Product Validations. Donald W. Hillger, Timothy J. Schmit, September 2007

NESDIS 126 A QA/QC Manual of the Cooperative Summary of the Day Processing System. William E. Angel, January 2008.

NESDIS 127 The Easter Freeze of April 2007: A Climatological Perspective and Assessment of Impacts and Services. Ray Wolf, Jay Lawrimore, April 2008.

NESDIS 128 Influence of the ozone and water vapor on the GOES Aerosol and Smoke Product (GASP) retrieval. Hai Zhang, Raymond Hoff, Kevin McCann, Pubu Ciren, Shobha Kondragunta, and Ana Prados, May 2008.

NESDIS 129 Calibration and Validation of NOAA-19 Instruments. Tsan Mo and Fuzhong Weng, editors, July 2009.

NESDIS 130 Calibration of the Advanced Microwave Sounding Unit-A Radiometer for METOP-B. Tsan Mo, August 2010.

NESDIS 131 The GOES-14 Science Test: Imager and Sounder Radiance and Product Validations. Donald W. Hillger and Timothy J. Schmit, August 2010.

NESDIS 132 Assessing Errors in Altimetric and Other Bathymetry Grids. Karen M. Marks and Walter H.F. Smith, January 2011.

NESDIS 133 The NOAA/NESDIS Near Real Time CrIS Channel Selection for Data Assimilation and Retrieval Purposes. Antonia Gambacorta and Chris Barnet, August 2011.

NESDIS 134 Report from the Workshop on Continuity of Earth Radiation Budget (CERB) Observations: Post-CERES Requirements. John J. Bates and Xuepeng Zhao, May 2011.

NESDIS 135 Averaging along-track altimeter data between crossover points onto the midpoint gird: Analytic formulas to describe the resolution and aliasing of the filtered results. Chang-Kou Tai, August 2011.

NESDIS 136 Separating the Standing and Net Traveling Spectral Components in the Zonal-Wavenumber and Frequency Spectra to Better Describe Propagating Features in Satellite Altimetry. Chang-Kou Tai, August 2011.

NESDIS 137 Water Vapor Eye Temperature vs. Tropical Cyclone Intensity. Roger B. Weldon, August 2011.

NESDIS 138 Changes in Tropical Cyclone Behavior Related to Changes in the Upper Air Environment. Roger B. Weldon, August 2011.

NESDIS 139 Computing Applications for Satellite Temperature Datasets: A Performance Evaluation of Graphics Processing Units. Timothy F.R. Burgess and Scott F. Heron, January 2011.

NOAA SCIENTIFIC AND TECHNICAL PUBLICATIONS

The National Oceanic and Atmospheric Administration was established as part of the Department of Commerce on October 3, 1970. The mission responsibilities of NOAA are to assess the socioeconomic impact of natural and technological changes in the environment and to monitor and predict the state of the solid Earth, the oceans and their living resources, the atmosphere, and the space environment of the Earth.

The major components of NOAA regularly produce various types of scientific and technical information in the following types of publications

PROFESSIONAL PAPERS – Important definitive research results, major techniques, and special investigations.

CONTRACT AND GRANT REPORTS – Reports prepared by contractors or grantees under NOAA sponsorship.

ATLAS – Presentation of analyzed data generally in the form of maps showing distribution of rainfall, chemical and physical conditions of oceans and atmosphere, distribution of fishes and marine mammals, ionospheric conditions, etc.

TECHNICAL SERVICE PUBLICATIONS – Reports containing data, observations, instructions, etc. A partial listing includes data serials; prediction and outlook periodicals; technical manuals, training papers, planning reports, and information serials; and miscellaneous technical publications.

TECHNICAL REPORTS – Journal quality with extensive details, mathematical developments, or data listings.

TECHNICAL MEMORANDUMS – Reports of preliminary, partial, or negative research or technology results, interim instructions, and the like.

U.S. DEPARTMENT OF COMMERCE
National Oceanic and Atmospheric Administration
National Environmental Satellite, Data, and Information Service
Washington, D.C. 20233

NOAA Technical Report NESDIS 140

Microburst Nowcasting Applications of GOES

Kenneth L. Pryor
NOAA/NESDIS/STAR
5200 Auth Road
Camp Springs, MD 20746

Washington, DC
September 2011

U.S. DEPARTMENT OF COMMERCE
Rebecca Blank, Secretary (Acting)

National Oceanic and Atmospheric Administration
Dr. Jane Lubchenco, Under Secretary of Commerce for Oceans and Atmosphere
and NOAA Administrator

National Environmental Satellite, Data, and Information Service
Mary Kicza, Assistant Administrator

Microburst Nowcasting Applications of GOES

KENNETH L. PRYOR
Center for Satellite Applications and Research (NOAA/NESDIS), Camp Springs, MD

ABSTRACT

Recent testing and validation have found that the Geostationary Operational Environmental Satellite (GOES) microburst products are effective in the assessment and short-term forecasting of downburst potential and associated wind gust magnitude. Two products, the GOES sounder Microburst Windspeed Potential Index (MWPI) and a new bi-spectral GOES imager brightness temperature difference (BTD) product have demonstrated capability in downburst potential evaluation. A comparison study between the GOES Convective Overshooting Top (OT) Detection and MWPI algorithms has been completed for cases that occurred during the 2007 to 2009 convective seasons over the southern Great Plains. Favorable results of the comparison study include a statistically significant negative correlation between the OT minimum temperature and MWPI values and associated measured downburst wind gust magnitude. The negative functional relationship between the OT parameters and wind gust speed highlights the importance of updraft strength, realized by large convective available potential energy (CAPE), in the generation of heavy precipitation and subsequent intense convective downdraft generation. This paper provides an updated assessment of the GOES MWPI and GOES BTD algorithms, presents case studies demonstrating effective operational use of the microburst products, and presents results of a cross comparison study of the GOES-R overshooting top (OT) detection algorithm over the United States Great Plains region.

1. Introduction and Background

A suite of products has been developed and evaluated to assess hazards presented by convective downbursts (Fujita 1985, Wakimoto 1985) derived from the current generation of Geostationary Operational Environmental Satellite (GOES-11 to 13). The existing suite of GOES-sounder (Menzel et al. 1998) derived microburst products are designed to accurately diagnose risk based on conceptual models of favorable environmental profiles. Pryor and Ellrod (2004) outlined the development of a GOES sounder-derived wet microburst severity index (WMSI) product to assess the potential magnitude of convective downbursts over the eastern United States, incorporating convective available potential energy (CAPE) as well as the vertical theta-e difference (TeD) (Atkins and Wakimoto 1991) between the surface and mid-troposphere. However, as noted by Caracena and Flueck (1988), the majority of microburst days during Joint

Airport Weather Studies (JAWS) were characterized by environments intermediate between the dry and wet extremes (i.e. "hybrid"). The Microburst Windspeed Potential Index (MWPI) is designed to quantify the most relevant factors in convective downburst generation in intermediate thermodynamic environments by incorporating: 1) CAPE, 2) the sub-cloud lapse rate between the 670 and 850-mb levels, and 3) the dew point depression difference between the typical level of a convective cloud base near 670 mb and the sub-cloud layer at 850 mb. The MWPI is a predictive linear model developed in the manner exemplified in Caracena and Flueck (1988) and consists of a set of predictor variables (i.e. dewpoint depression, temperature lapse rate) that generates output of expected microburst risk. Analysis of microbursts during the JAWS project (Wakimoto 1985; Caracena and Flueck 1988) identified the following favorable environmental characteristics: 1) low surface dew-point temperatures, 2) high convective cloud base, 3) low 500-mb dewpoint temperature depression, 4) high subcloud lapse rate. Thus, the MWPI algorithm that accounts for both updraft (**U**) and downdraft instability (**D**) in microburst generation is defined as

$$\mathrm{MWPI} \equiv \underbrace{\{(\mathrm{CAPE}/100)\}}_{\mathbf{U}} + \underbrace{\{\Gamma + (T\text{-}T_d)_{850} - (T\text{-}T_d)_{670}\}}_{\mathbf{D}} \qquad (1)$$

where Γ is the lapse rate in degrees Celsius (C) per kilometer from the 850 to the 670 mb level, and the quantity $(T–T_d)$ is the dewpoint depression (C). Due to the dependence of storm precipitation content on CAPE and the resulting contribution of positive buoyancy to precipitation loading, updraft instability can be translated into downdraft instability. Thus, the CAPE factor could also be considered a downdraft instability term. The MWPI algorithm is expected to be most effective in assessing downburst wind gust potential associated with "pulse"-type (short duration, single cell) convective storms in weak wind shear environments.

Generation of the MWPI product is based on the following assumptions:

- Precipitation is initially in the form of graupel.
- Sub-cloud phase-change cooling (especially evaporation) is the primary forcing factor in negative buoyancy generation and subsequent acceleration of convective storm downdrafts. Precipitation loading is a secondary forcing mechanism.
- The convective storm cloud base and freezing level are located at or above the 670 mb level.

In a prototypical dry microburst environment, Wakimoto (1985) identified a convective cloud base height near 500 mb associated with an "inverted V" profile. In contrast, Atkins and Wakimoto (1991) identified a typical cloud base height in a pure wet microburst environment near 850 mb. Thus, a cloud base height of 670 mb was selected for a hypothetical, weak shear intermediate microburst environment. This selection agrees well with the mean level of free convection (LFC) of 685 mb inferred from the inspection of 51 GOES proximity soundings corresponding to downburst events that occurred in Oklahoma and western Texas between 1 June 2007 and 31 August 2008. The median LFC was 685 mb and mode LFC computed for the 2007-2008 convective seasons was 670 mb. The selection of 670 mb as the prototypical cloud base height over the southern Plains was affirmed by the majority of LFCs observed between 670 and 700 mb. In addition, comparison of 78 recorded downburst events over Oklahoma and western Texas during the 2009 convective season to proximity Rapid Update Cycle (RUC) sounding profiles resulted in calculated mean, median, and mode LFCs of 700 mb. Furthermore, Schafer (1986) noted that along the western periphery of the dryline in an environment with westerly geostrophic flow (favorable background flow in the dryline environment), the top of the mixed layer is typically found near 670 mb. In a free convective regime (i.e. light winds, no

convective inhibition (CIN)), the mode LFC of 670 mb can be considered representative of convective cloud base heights in an intermediate microburst environment such that LFC ≈ LCL ≈ z_i ≈ 670 mb, where LCL is the lifting condensation level and z_i represents mixed layer depth. Johns and Doswell (1992) identified necessary ingredients for deep convection:

- A moist layer of sufficient depth in the low or mid troposphere
- A steep lapse rate to allow for a substantial "positive area" or CAPE

CAPE has an important role in precipitation formation due to the strong dependence of updraft strength and resultant storm precipitation content on positive buoyant energy. Loading of precipitation, typically in the form of graupel, initiates the convective downdraft. The subsequent melting of graupel and sub-cloud evaporation of rain result in cooling and the negative buoyancy that accelerate the downdraft in the unsaturated layer. Collectively, melting of graupel, subsequent evaporative cooling and resulting downdraft strength are enhanced by large liquid water content and related water surface available for evaporation, and a steep lapse rate that acts to maintain negative buoyancy as the downdraft descends in the sub-cloud layer. The intense downdraft subsequently produces strong and potentially damaging winds upon impinging on the surface. Ellrod (1989) noted that lapse rates, specifically between 700 and 850 mb, contained the most predictive information for determining downburst potential using GOES sounder profile data. In addition, Caplan et al. (1990) noted that afternoon sub-cloud temperature lapse rates were strongly correlated with microburst activity. Derivation of the MWPI algorithm is primarily based on parameter evaluation and pattern recognition techniques as employed in the severe convective storm forecasting process (Johns and Doswell 1992).

Although the MWPI algorithm was originally designed for convective wind speed potential assessment in intermediate thermodynamic environments over the central United States, the MWPI

has demonstrated potential effectiveness for both wet microbursts that occur over the southeastern U.S. as well as for dry microbursts that occur over the intermountain West. For wet microburst environments, large CAPE and steep lapse rates between the 700 and 850 mb levels would be readily detected by the MWPI algorithm. Precipitation loading, melting of hail, and evaporation of liquid precipitation in the layer between 700 and 850 mb would enhance negative buoyancy and resulting downdraft acceleration in wet-microburst producing convective storms. For dry microburst environments, where cloud bases are typically above the freezing level, sublimational cooling of frozen precipitation will enhance negative buoyancy and downdraft acceleration. The temperature lapse rate and dewpoint depression difference terms effectively indicate a favorable boundary layer thermodynamic structure for microbursts in a low CAPE environment.

In addition, it has been found recently that the brightness temperature difference ("BTD") between GOES infrared band 3 (water vapor, 6.5μm) and band 4 (thermal infrared, 11μm) can highlight regions where severe outflow wind generation (i.e. downbursts, microbursts) is likely due to the channeling of dry mid-tropospheric air into the precipitation core of a deep, moist convective storm. Rabin et al. (2010) noted that observations have shown that BTD > 0 can occur when water vapor exists above cloud tops in a stably stratified lower stratosphere and thus, BTD > 0 has been used a measure for intensity of overshooting convection. A new feature presented in this paper readily apparent in BTD imagery is a "dry-air notch", identified in GOES infrared imagery as a V- or U-shaped region of relatively warm brightness temperature that typically appears on the rear flank of microburst-producing convective storms. The graphical depiction in Figure 1a shows that the dry-air notch can signify the development of a microburst as dry air is being channeled into the convective storm core. The dry-air notch has been associated with numerous significant microburst events over the past decade.

A comparison study between the GOES Convective Overshooting Top (OT) Detection and MWPI algorithms has been completed for cases that occurred during the 2007 to 2009 convective seasons over the southern Great Plains. The OT detection algorithm (Bedka et al. 2010) is a pattern recognition-based technique that employs brightness temperature (BT) data from the GOES thermal infrared channel. Output OT detection algorithm parameters include cloud top minimum BT and a BT difference between the overshooting top and surrounding convective anvil cloud. This report will provide an assessment of the GOES MWPI and GOES BTD algorithms, presents case studies demonstrating effective operational use of the microburst products, and presents results of the intercomparison study of the GOES-R overshooting top (OT) detection algorithm over the United States Great Plains region.

2. Data collection and methodology

a. GOES Microburst Products

The main objective of the validation effort is to qualitatively and quantitatively assess and intercompare the performance of the MWPI and BTD algorithms by employing classical statistical analysis of real-time data. Accordingly, this effort entails a study of downburst events in a manner that emulates historic field projects such as the 1982 Joint Airport Weather Studies (JAWS) (Wakimoto 1985) and the 1986 Microburst and Severe Thunderstorm (MIST) project (Atkins and Wakimoto 1991). Algorithm output data was collected for downburst events that occurred during the warm season (especially between 1 June and 30 September) and was validated against surface observations of convective wind gusts as recorded by reliable surface observation stations in mesoscale networks. Wakimoto (1985) and Atkins and Wakimoto (1991) discussed the effectiveness of using mesonetwork surface observations and radar reflectivity data in the verification of the occurrence of downbursts. Site characteristics, data quality assurance, and wind

sensor calibration are thoroughly documented in Brock et al. (1995) and Schroeder et al. (2005).Well-defined peaks in wind speed as well as significant temperature decreases (Wakimoto 1985; Atkins and Wakimoto 1991) were effective indicators of high-reflectivity downburst occurrence.

As illustrated in the flowchart in Figure 1b, MWPI product images are generated by Man computer Interactive Data Access System (McIDAS)-X. This program reads and processes GOES sounder data, calculates and collates microburst risk values, and overlays risk values on GOES imagery. Output images are then archived via FTP and HTTP to the GOES Microburst Products web page. For selected downburst events, the MWPI product was generated using the Graphyte Toolkit and McIDAS-V (Available online at http://www.ssec.wisc.edu/mcidas/software/v/). The MWPI algorithm, as implemented in the Graphyte Toolkit, reads and processes GOES sounder profile data in binary format available on the GOES sounding profile web page (http://www.star.nesdis.noaa.gov/smcd/opdb/goes/soundings/html/sndbinary23L.html). The MWPI is then calculated for each retrieval location and plotted as a colored marker on a user-defined map.

The BTD product consisted of image data derived brightness temperatures from GOES-East (GOES-12, 2009 and before; GOES-13, 2010 and after) 4-km resolution water vapor (band 3) and thermal infrared (band 4), obtained from the Comprehensive Large Array-data Stewardship System (CLASS, http://www.class.ncdc.noaa.gov/). Microburst algorithm output was visualized by McIDAS-V. A data stretch and built-in color enhancement ("Pressure") were applied to the output images to highlight patterns of interest including overshooting tops and dry-air notches. The dry -air notch identified in the BTD image is analogous in concept to the rear-

inflow notch (RIN) as identified in radar imagery and documented in Przybylinski (1995). Next Generation Radar (NEXRAD) and Terminal Doppler Weather Radar (TDWR) base reflectivity imagery from National Climatic Data Center (NCDC) were utilized to verify that observed wind gusts are associated with high-reflectivity downbursts and not associated with other types of convective wind phenomena (i.e. gust fronts). An application of radar imagery is to infer microscale physical properties of downburst-producing convective storms. Particular radar reflectivity signatures, such as the rear-inflow notch (RIN)(Przybylinski 1995) and the spearhead echo (Fujita and Byers 1977), are effective indicators of the occurrence of downbursts.

Since surface data quality is paramount in an effective validation program, relatively flat, treeless prairie regions were chosen as study regions. The treeless, low-relief topography that dominates sparsely populated regions such as the U.S. High Plains allowed for the assumption of horizontal homogeneity when deriving a conceptual model of a boundary layer thermodynamic structure favorable for downbursts. More importantly, planar topography and water body surfaces facilitate relatively smooth flow (due to small surface roughness) with respect to downburst winds in which drag and turbulent eddy circulation resulting from surface obstructions (i.e., buildings, hills, and trees) are minimized. Sorbjan (1989) describes the wind profile in the surface layer and dictates that the relatively small roughness parameter of short grass prairie would permit wind gust measurements that are more representative of downburst intensity. Over the eastern United States, coastal and estuarine waters are optimal for a validation study. Observational data from Integrated Ocean Observing System (IOOS) stations (http://www.ioos.gov/catalog/) and WeatherFlow (http://datascope.weatherflow.com/) was preferred for algorithm validation. One particular wind sensor, mounted on the Potomac River buoy owned and operated by Intellicheck Mobilisa, was employed for the purpose of an in-depth study of the physical structure of downbursts and

microbursts in addition to product validation. The wind sensor computes wind speed and direction using an ultrasonic retrieval method in which quantities are calculated as a scalar average of all samples over a ten-second averaging time. This results in very accurate wind measurements that are more likely to represent the true character of convectively-generated winds.

In order to assess the predictive value of the algorithm output, the closest representative index values were obtained for retrieval times one to three hours prior to the observed surface wind gusts. Representativeness of proximate index values was ensured by determining from analysis of surface observations, radar, and satellite imagery that no change in environmental static stability and air mass characteristics between product valid time and time of observed downbursts had occurred. Furthermore, in order for the downburst observation to be included in a validation data set, it was required that the parent convective storm cell of each downburst, with radar reflectivity greater than 35 dBZ, be located nearly overhead at the time of downburst occurrence. An additional criterion for inclusion into a data set is a wind gust measurement of at least F0 intensity (35 knots) on the Fujita scale (Fujita 1971). Wind gusts of 35 knots or greater are considered to be operationally significant for transportation, especially boating and aviation. A technique devised by Wakimoto (1985) to visually inspect wind speed observations over the time intervals encompassing candidate downburst events was implemented to exclude gust front events from the validation data set. In summary, the screening process employed to build the validation data set that consists of criteria based on surface weather observations and radar reflectivity data yielded a statistically significant sample size of downbursts and associated index values. This validation data set is presented graphically in the scatterplot in Figure 17.

Covariance between the variables of interest, MWPI and surface downburst wind gust speed, was considered. Algorithm effectiveness was assessed as the correlation between MWPI

values and observed surface wind gust velocities. Statistical significance testing was conducted to determine the confidence level of the correlation between observed downburst wind gust magnitude and microburst risk values. Examples of MWP and BTD algorithm validation employing the direct comparison method are shown graphically in Section 3.

b. GOES Overshooting Top Detection Algorithm

A comparison study between the GOES Convective Overshooting Top (OT) Detection and MWPI algorithms has also been completed for cases that occurred during the 2007 to 2009 convective seasons over the southern Great Plains. The OT detection algorithm (Bedka et al. 2010) is a pattern recognition-based technique that employs brightness temperature (BT) data from the GOES infrared window (IRW) channel. Dworak et al. (2011) describes the OT detection method as follows: (1) Relative BT minima that are lower than 215 K are first identified and then compared to an NWP tropopause temperature to verify that the pixels are indeed cloud tops "overshooting" through the tropopause region. (2) Checks are then performed to ensure that no minima are located within 15 km of each other so that portions of the same OT are not classified as two independent tops. (3) The IRW BT of the anvil cloud surrounding the potential OT is then sampled at an ~8 km radius in 16 directions and must have an IRW temperature at or colder than 225 K to be included in the mean computation. The 225 K threshold is important to ensure that only non-overshooting anvil pixel BTs are included in the mean anvil temperature computation. (4) At least 5 valid anvil pixels must be present to ensure that the anvil is of relatively large horizontal extent but allows an anvil to occupy as small as a 90° quadrant, which might be the case when strong jet-level winds are present. (5) A pixel is classified as an overshooting top if it is $\geq$ 6.5 K colder than the mean BT of the surrounding anvil cloud. The OT detection algorithm is intended to fulfill a requirement for the GOES-R

Advanced Baseline Imager (ABI) instrument. GOES-R is scheduled for launch in 2015 and should be operational by 2017. Output OT detection algorithm parameters that include cloud top minimum BT and a BT difference between the overshooting top and surrounding convective anvil cloud have been compared to the closest representative MWPI values and the closest measured downburst wind gusts within 20 km and 20 minutes by Oklahoma and West Texas Mesonet stations. Close correspondence between the location of overshooting tops, proximate MWPI values, and the location of observed downburst winds are evident in section 3a.

3. Case Studies

a. August 2009 Oklahoma Downbursts

During the afternoon of 10 August 2009, strong convective storms developed along a cold front that extended from eastern Kansas to the Oklahoma Panhandle. The storms tracked eastward and produced several strong downbursts over northwestern and north-central Oklahoma during the late afternoon and evening. Table 1 features a listing of five significant high wind measurements by Oklahoma Mesonet stations during this downburst event. The last and highest downburst wind gust of the event, 33 ms^{-1} (64 kt), was recorded at Freedom station at 2345 UTC. It was found that the GOES MWPI, BTD and OT detection algorithms were effective in indicating the intensity of convective storm activity and resulting downburst wind gust magnitude. A correlation of 0.83 between MWPI values and measured wind gusts and a correlation of -0.88 between OT minimum BT and measured wind gusts exemplified the strong statistical relationship between these parameters and downburst wind gust magnitude.

At 2200 UTC, Figure 2a, the MWPI product image displayed elevated values widespread over Kansas and Oklahoma with high values (red) that indicate wind gust potential greater than 50 knots (25 ms^{-1}) over northwestern Oklahoma and southern Kansas, in the vicinity of the

developing convective storm activity. Along and immediately ahead of the cold front, moderate (yellow) values indicated wind gust potential of 18 to 25 ms^{-1} (35 to 49 kt). Downburst wind gusts recorded by mesonet stations between 2115 and 2305 UTC ranged from 20 to 23 ms^{-1} (40 to 45 kt), consistent with gust potential as shown in the 2200 UTC MWPI product. An intrusion of dry mid-tropospheric air was becoming apparent on the western flank of the developing convective storm complex over the eastern Oklahoma Panhandle and extreme southern Kansas. Figure 2b, the Graphyte visualization of the 2200 UTC MWPI, shows a general increase in index values from west to east over northwestern Oklahoma and southern Kansas. Figure 2b is also effective in highlighting that the Freedom downburst occurred in proximity to a local maximum in MWPI (near 60, red marker) just north of the Kansas-Oklahoma border.

A dry air notch had become especially well-defined on the northwestern flank of a convective storm in phase with a RIN as apparent in radar imagery and shown in the 2302 UTC BTD image in Figure 3a. Note that in Figure 3a, the overshooting top was co-located with a maximum in radar reflectivity and located 13 km northeast of the Buffalo (BUFF) mesonet station, where a downburst wind gust of 23 ms^{-1} (45 kt) was recorded at 2305 UTC. During the next 30 minutes, the multicellular storm intensified as it tracked eastward toward higher CAPE (3074) and MWPI (51.7) values southeast of Freedom (FREE). At 2345 UTC, a much stronger downburst was recorded at Freedom mesonet station. The cold overshooting top BT value of 196°K, located 13 km northwest of Freedom, was associated with the severe downburst, highlighting the importance of convective storm updraft strength in the generation of severe weather, especially high winds. In a similar manner to the previous OT, the OT near Freedom was co-located with a maximum in reflectivity (> 65 dBZ). The closest representative MWPI value of 52 corresponded to wind gust potential of 25 to 33

ms^{-1} (50 to 64 kt). A dry air notch, apparent in the BTD image as a light-to-dark blue shaded indentation, illustrated the role and importance of the entrainment of dry, mid-tropospheric air into the rear flank of the convective storm and the subsequent generation of intense downdrafts. The displacement between the dry-air notch and the RIN identified in radar imagery was likely due to the 11-minute time difference between the satellite and radar images.

The favorable environment for downbursts was well illustrated in Figure 4, the 0000 UTC (11 August) radiosonde observation from Dodge City, Kansas. Large CAPE and a large temperature lapse rate below the 550-mb level were instrumental in fostering a strong storm updraft that was realized as a heavy precipitation core and overshooting tops observed at 2302 and 2332 UTC over northwestern Oklahoma. In addition, the sounding indicated the presence of two prominent dry-air layers centered near the 400-mb and 700-mb levels. Strong westerly winds of 20 to 25 ms^{-1} (40 to 50 kt) were measured in the upper dry-air layer that likely injected this dry air into the storm precipitation core that enhanced downdraft acceleration and subsequent severe winds observed on the surface by the Freedom mesonet station. As described in the introduction, interaction of mid-tropospheric dry air with the precipitation core likely resulted in cooling due to evaporation of precipitation that fostered negative buoyancy and the acceleration of the downdraft toward the surface. All of these favorable conditions were reflected in the 2332 UTC composite GOES-NEXRAD image that displayed concurrent high storm radar reflectivity, an overshooting top, a high MWPI value, and a prominent dry-air notch on the western flank of the storm.

b. June 2010 West Texas Downbursts

During the afternoon of 22 June 2010, an upper-level disturbance interacted with a dryline near the Texas-New Mexico border and triggered strong convective storms that tracked

eastward into the western Texas Panhandle region. Convective storms produced scattered strong downbursts over western Texas during the evening hours. Figure 5, the 2300 UTC GOES MWPI product image, effectively indicated the potential for strong downbursts two to three hours prior to each event. Surface wind observation data from West Texas Mesonet was instrumental in verifying downburst intensity during this event.

The MWPI product performed especially well during the evening of 22 June. Figure 5 shows that the 2300 UTC MWPI product image, visualized by both McIDAS and Graphyte, indicated elevated values near the Texas-New Mexico border, west of longitude 102°W, and a local maximum near Muleshoe (orange to red shading in Graphyte) with index values of 40 to 45. Figure 5a shows a line of enhanced cumulus clouds forming along the dryline over the Texas-New Mexico border. As an upper-level disturbance interacted with the dryline, convective storms intensified and then tracked into western Texas after 0000 UTC. Comparing the McIDAS and Graphyte versions of the MWPI product, it is evident that the Graphyte visualization more effectively highlighted enhanced downburst wind speed potential over extreme western Texas, near the New Mexico border. The corresponding GOES sounding profile in Figure 7 displays a favorable classic "inverted V" profile that prevailed over western Texas. A deep dry adiabatic lapse rate (DALR) layer below the 670-mb level and a dry subcloud layer fostered intense downdraft development due to evaporational cooling and resultant negative buoyancy generation. Upon impact of the intense downdrafts on the surface, strong downburst winds were generated. The MWPI product was particularly effective as index values of 40 to 45 corresponded to measured downburst wind gusts of 23.7 ms^{-1} (46 kt) at Hereford at 0110 UTC and 22.1 ms^{-1} (43 kt) at Muleshoe at 0120 UTC 23 June. Based on the established statistical relationship shown in Figure 17, MWPI values of 40 to 45 correspond to wind gust

potential of 23 to 25 ms^{-1} (46 to 48 kt). Figure 6, composite GOES-NEXRAD images at 0110 and 0125 UTC 23 June, shows that as the broken line of convective storms tracked eastward over the Texas-New Mexico border, particularly well defined dry-air notches became apparent over eastern New Mexico on the western flank of the line. The dry-air notches were oriented toward the east and southeast, toward intense cells that were producing strong downburst winds over Hereford and Muleshoe. As in the previous case, these dry-air notches, in line with RINs, as identified in radar reflectivity imagery, signified the channeling of dry mid-tropospheric air into heavy precipitation cores. The interaction of this dry air with the heavy precipitation resulted in the generation of strong negative buoyancy and subsequent intense downdrafts. The overlay of MWPI values in both images highlight the correlation between MWPI and measured downburst wind gusts with a value of 40.5 indicated near Muleshoe and a value of 43 indicated near Hereford. As the convective line continued to track east into a more stable region with lower CAPE and MWPI values, no further significant downburst activity occurred.

c. May 2011 Hampton Roads Downbursts

During the afternoon of 24 May 2011, a multicellular convective storm developed over the southern piedmont of Virginia and tracked rapidly eastward toward the lower Chesapeake Bay. Between 2000 and 2100 UTC, as the convective storm passed over the Hampton Roads, one of the busiest waterways in the continental U.S., numerous severe wind gusts were recorded by WeatherFlow (WF) and Physical Oceanographic Real-Time System (PORTS) stations. After inspecting satellite and radar imagery for this event, it was apparent that these severe wind observations were associated with downburst activity. GOES MWPI imagery in Figure 8 indicated a general increase in wind gust potential over the Hampton Roads area during the afternoon hours. The increase in both convective and downdraft instability was reflected in the

Norfolk, Virginia GOES sounding profile in Figure 9 as a marked increase in CAPE and an elevation and increasing amplitude of the mid-tropospheric dry-air layer. By 2000 UTC, the McIDAS visualization of the MWPI product indicated the highest wind gust potential, up to 33 ms^{-1} (64 kt), over Hampton Roads, where wind gusts of 29 to 35 ms^{-1} (57 to 67 kt) were recorded by WeatherFlow and PORTS stations during the following hour. Table 2 lists the most significant wind observations associated with severe thunderstorm event. Visible imagery emphasized the multicellular structure of the storm with overshooting tops identifying the most intense convective cells that were capable of producing severe downbursts. Figure 10 illustrates the observing network over the Hampton Roads area that revealed the divergent nature of the downburst winds as the storm was tracking overhead. Figure 11a, the composite GOES-NEXRAD image at 2025 UTC, with overlying MWPI values, revealed favorable conditions for severe downbursts with prominent dry-air notches on the southwestern and northwestern flanks of the storm pointing toward the convective precipitation core. This signifies that the entrained mid-tropospheric dry air was interacting with the storm precipitation core to result in evaporational cooling, negative buoyancy generation, and subsequent acceleration of storm downdrafts. Similar to the August 2009 case, GOES sounding profiles reflected elevated MWPI values by displaying the presence of large CAPE, a dry sub-cloud layer, and a steep temperature lapse rate below the 700-mb level. By 2040 UTC, as shown in Figure 11b, dry-air notches had become more pronounced in BTD imagery while prominent spearhead echoes were apparent in radar imagery. Near this time, significant severe downburst winds were recorded by PORTS and WeatherFlow stations on the Chesapeake Bay Bridge-Tunnel between Virginia Beach and Cape Charles. As the storm moved eastward over the Virginia Beach oceanfront, weaker downburst winds were recorded by the Sandbridge WeatherFlow station where wind gust potential of 18 to

25 ms^{-1} (35 to 49 kt) was indicated at 2000 UTC. The Graphyte visualization for this case more effectively displayed wind gust potential along the Atlantic coast from Virginia Beach southward, where a local maximum value of 47 (dark red cross east of Manteo, North Carolina) corresponded to a downburst wind gust of 24.2 ms^{-1} (47 kt) recorded at Sandbridge at 2050 UTC.

d. August 2011 Chesapeake Bay Downbursts

During the afternoon of 25 August 2011, a line of convective storms developed over the Blue Ridge Mountains ahead of a cold front and then tracked rapidly southeastward over the lower tidal Potomac River and Chesapeake Bay. Between 2110 and 2130 UTC, as a convective storm line was moving over the tidal Potomac River near Dahlgren, Virginia and the Nice Memorial Bridge, a strong downburst was observed by the wind sensor on the Potomac River buoy. A peak wind of 22.6 ms^{-1} (44 kt) was measured by the buoy as a bow echo, embedded in a multicellular convective storm, passed nearly overhead. Over the next hour, downburst wind gusts between 19 and 24 ms^{-1} (37 and 47 kt) were recorded by PORTS stations on the lower tidal Potomac River and the Chesapeake Bay. The late afternoon (2100 UTC) GOES MWPI product, shown in Figure 12, indicated elevated downburst risk ahead of the convective storm line over the lower Chesapeake Bay. Similar to the Hampton Roads case, a prominent overshooting top was apparent in visible GOES imagery just east of the Potomac River buoy at the time of downburst occurrence. Favorable conditions for downbursts were reflected in Figure 13, the corresponding GOES sounding profile over Patuxent River Naval Air Station in southern Maryland. Similar to the previous studies, especially apparent over Oklahoma and Virginia, large CAPE and the presence of a mid-tropospheric dry-air layer were major factors highlighted in the sounding. The composite GOES-NEXRAD images in Figure 14, visualized near the time of downburst occurrence, captured

a major forcing factor of downburst generation by indicating the presence of well-defined dry-air notches on the northwestern flank of the convective storm line.

Figure 14 also shows elevated values (27 to 36) downstream of the intense convective storm line tracking through the tidal Potomac River region. MWPI values of 27 to 36 correlate to wind gust potential of 22 to 23 ms^{-1} (43 to 45 kt). The wind histogram from the Potomac River buoy in Figure 15 shows that near 2120 UTC, a peak wind of 22.6 ms^{-1} (44 kt) was recorded as the convective storm passed nearly overhead. The high-resolution histogram, derived from 10-second wind observations, reveals a more realistic structure and turbulent character of downburst wind flow, with sharply-defined lulls and peaks in the wind superimposed over a general increase in wind speed observed as the convective storm tracked overhead. The peaks in wind speed, recorded by the buoy between 2110 and 2130 UTC, likely indicate the passage of roll vortices and smaller microbursts embedded within the larger scale downburst wind flow. This case is important to show that downburst winds are not always characterized by a single peak in wind speed, as demonstrated with 6-minute time resolution PORTS observations displayed in Figure 16, but, rather, by several wind peaks superimposed over the convective storm outflow.

In addition, composite imagery in Figure 14 shows that between 2115 and 2215 UTC the convective storm line became more solid as it tracked southeastward toward the Chesapeake Bay and featured a prominent leading convective line and a trailing stratiform precipitation region. Within this organized convective storm system, spearhead echoes were still apparent near the location of downburst winds that were recorded by PORTS stations between 2212 and 2230 UTC at Piney Point (1), Solomons Island (2), and Cove Point (3). The dry-air notches on the northwestern flank of the storm pointing toward the buoy and the lower Tidal Potomac River signified that entrained dry air was interacting with the storm precipitation cores to result in

evaporational cooling, negative buoyancy generation, and subsequent acceleration of storm downdrafts. As the convective storm line continued to track southeastward toward the lower Chesapeake Bay, no further significant downburst activity occurred. Significant wind observations recorded during this downburst event are displayed in Figure 16 and noted in Table 3.

4. Discussion

a. Validation Results

Validation results for the 2007 to 2010 convective seasons have been completed for the MWPI product. GOES sounder-derived MWPI values have been compared to mesonet observations of downburst winds over Oklahoma and Texas for 208 events between June 2007 and September 2010. The correlation between MWPI values and measured wind gusts was determined to be 0.62 and was found to be statistically significant near the 100% confidence level, indicating that the correlation represents a physical relationship between MWPI values and downburst magnitude and is not an artifact of the sampling process. Figure 17 shows a scatterplot of MWPI values versus observed downburst wind gust speed as recorded by mesonet stations in Oklahoma and Texas. The MWPI scatterplot identifies two clusters of values: MWPI values less than 50 that correspond to observed wind gusts between 18 to 26 ms^{-1} (35 to 50 kt), and MWPI values greater than 50 that correspond to observed wind gusts greater than 26 ms^{-1} (50 kt). The scatterplot illustrates the effectiveness of the MWPI product in distinguishing between severe and non-severe convective wind gust potential.

The comparison study between the GOES-R Convective Overshooting Top (OT) Detection and MWPI algorithms has also produced favorable results, shown in Figure 18, that include a statistically significant negative correlation between the OT minimum temperature and

MWPI values (r=-0.47) and OT temperature and measured wind gust magnitude (r=-0.39) for 47 cases that occurred between 2007 and 2009. The negative functional relationship between the OT parameters and wind gust speed highlights the importance of updraft strength, realized by large CAPE, in the generation of heavy precipitation and subsequent intense convective downdraft generation. These results are consistent with the findings of Dworak et al. (2011) that show a near- linear relationship between overshooting top BT and magnitude and severe wind frequency (Figure 18a,b).

b. Limitations

Due to the dependence of the MWPI algorithm on the availability of GOES sounding retrievals, MWPI values are calculated and plotted only in regions of clear skies or partial cloudiness. Thus, extrapolation of MWPI values may be required in cloud-covered regions. Also, the MWPI is designed for use with quasi-stationary, pulse-type convective storms. When applying the MWPI product to migratory convective storms, it is important to account for the translational motion of the storms of interest in assessing wind gust potential.

5. Conclusions

As documented in Pryor (2008, 2010), and proven by statistical analysis, the GOES sounder MWPI product has demonstrated capability in the assessment of wind gust potential over the southern Great Plains and Mid-Atlantic coast regions. Statistical analysis for downburst events that occurred during the 2007 to 2010 convective seasons and case studies from the 2009 to 2011 convective seasons demonstrated the effectiveness of the GOES microburst products. However, as noted by Caracena and Flueck (1988), the majority of microburst days during JAWS were characterized by environments intermediate between the dry and wet extremes (i.e. hybrid). As explained in Pryor (2008), the MWPI product is especially useful in the inference of

the presence of intermediate or "hybrid" microburst environments, especially over the Great Plains region. Further validation over the Atlantic coast region should strengthen the functional relationship between MWPI values and downburst wind gust magnitude.

The dry-air notch identified in both case studies presented above likely represents drier (lower relative humidity) air that is entrained into the rear of convective storms and interacts with their precipitation cores, subsequently providing the energy for intense downdrafts and resulting downburst winds. Comparison of BTD product imagery to corresponding radar imagery revealed physical relationships between the dry-air notch, rear-inflow notch (RIN) and the spearhead echo. Entrainment of drier mid-tropospheric air into the precipitation core of the convective storm typically results in evaporation of precipitation, the subsequent cooling and generation of negative buoyancy (sinking air), and resultant acceleration of a downdraft. When the intense localized downdraft reaches the surface, air flows outward as a downburst. Ellrod (1989) noted the importance of low mid-tropospheric (500-mb) relative humidity air in the generation of the severe Dallas-Fort Worth, Texas microburst in August 1985. Thus, the band 3-4 BTD product can serve as an effective supplement to the GOES sounder MWPI product, especially in regions where there is no Doppler radar coverage (i.e. over open ocean waters). Further validation of the imager microburst product and quantitative statistical analysis to assess product performance will serve as future work in the development and evolution of the GOES microburst products.

Acknowledgements. The author thanks Kristopher Bedka (Science Systems and Applications, Inc.) for the overshooting top detection algorithm output dataset used in the intercomparison study. The author also thanks the Oklahoma and West Texas Mesonets, Jay Titlow (WeatherFlow), and John Krouse (Intellicheck Mobilisa) for the surface weather observation data used in this research effort. The author thanks Michael Grossberg and Paul Alabi (NOAA/CREST, CCNY) for their implementation of the MWPI program into the Graphyte Toolkit and their assistance in generating the MWPI product images and Jaime Daniels (NESDIS) for providing GOES sounding retrievals displayed in this paper.

REFERENCES

Atkins, N.T., and R.M. Wakimoto, 1991: Wet microburst activity over the southeastern United States: Implications for forecasting. *Wea. Forecasting*, **6**, 470-482.

Bedka, K., J. Brunner, R. Dworak, W. Feltz, J. Otkin, and T. Greenwald, 2010: Objective Satellite-Based Detection of Overshooting Tops Using Infrared Window Channel Brightness Temperature Gradients. *J. Appl. Meteor. Climatol.*, **49**, 181–202.

Brock, F. V., K. C. Crawford, R. L. Elliott, G. W. Cuperus, S. J. Stadler, H. L. Johnson and M. D. Eilts, 1995: The Oklahoma Mesonet: A technical overview. *Journal of Atmospheric and Oceanic Technology*, **12**, 5-19.

Caplan, S.J., A.J. Bedard, and M.T. Decker, 1990: The 700–500 mb Lapse Rate as an Index of Microburst Probability: An Application for Thermodynamic Profilers. *Journal of Applied Meteorology*, **29**, 680–687.

Caracena, F., and J.A. Flueck, 1988: Classifying and forecasting microburst activity in the Denver area. *J. Aircraft*, **25**, 525-530.

Dworak, R., K. M. Bedka, J. Brunner, and W. Feltz, 2011: Comparison between GOES-12 overshooting top detections, WSR-88D radar reflectivity, and severe storm reports. Submitted to *Wea. Forecasting.*

Ellrod, G. P., 1989: Environmental conditions associated with the Dallas microburst storm determined from satellite soundings. *Wea. Forecasting*, **4**, 469-484.

Fujita, T.T., 1971: Proposed characterization of tornadoes and hurricanes by area and intensity. SMRP Research Paper 91, University of Chicago, 42 pp.

Fujita, T.T., 1985: The downburst, microburst and macroburst. SMRP Research Paper 210, University of Chicago, 122 pp.

Fujita, T.T., and H.R. Byers, 1977: Spearhead echo and downburst in the crash of an airliner. *Mon. Wea. Rev.*, **105**, 129–146.

Johns, R.H., and C.A. Doswell, 1992: Severe local storms forecasting. *Mon. Wea. Rev.*, **121**, 1134–1151.

Menzel, W.P., F. Holt, T. Schmit, R. Aune, A. Schreiner, G. Wade, and D. Gray, 1998: Application of GOES 8/9 soundings to weather forecasting and nowcasting. *Bull. Amer. Meteor. Soc.*, **79**, 2059-2077.

Pryor, K.L., and G.P. Ellrod, 2004: WMSI - A new index for forecasting wet microburst severity. *National Weather Association Electronic Journal of Operational Meteorology*, 2004-EJ3.

Pryor, K. L., 2008: An Initial Assessment of the GOES Microburst Windspeed Potential Index. Preprints, 5th GOES Users' Conf., New Orleans, LA, Amer. Meteor. Soc.

Pryor, K. L., 2010: Recent developments in microburst nowcasting using GOES. Preprints, 17th Conference on Satellite Meteorology and Oceanography, Annapolis, MD, Amer. Meteor. Soc.

Przybylinski, R.W., 1995: The bow echo. Observations, numerical simulations, and severe weather detection methods. *Wea. Forecasting*, **10**, 203-218.

Rabin, R., P. Bothwell, and S. Weiss, 2010: Temperature deviation from Equilibrium Temperature: Convective Overshoot from Satellite Imagery. [Available online at http://overshoot.nssl.noaa.gov/.]

Schroeder, J.L., W.S. Burgett, K.B. Haynie, I. Sonmez, G.D. Skwira, A.L. Doggett, and J.W. Lipe, 2005: The West Texas Mesonet: A technical overview. *Journal of Atmospheric and Oceanic Technology*, **22**, 211-222.

Sorbjan, Z., 1989: Structure of the atmospheric boundary layer. Prentice Hall, 317pp.

Wakimoto, R.M., 1985: Forecasting dry microburst activity over the high plains. *Mon. Wea. Rev.*, **113**, 1131-1143.

TABLES AND FIGURES

Table 1. Measured wind gusts compared to MWPI values and OT properties for the 10 August 2009 Oklahoma downburst event. All times are in UTC.

Time	Gust Speed ms^{-1} (kt)	Location	MWPI	OT Time	OT Dist (km)	OT Min (°K)	OT Mag (°K)
2115	20.6 (40)	Copan	31	2115	9	206.5	-9.2
2125	22.1 (43)	Lahoma	44	2115	9	210.1	-7
2230	21.1 (41)	Slapout	33	2215	12	211.6	-8.7
2305	23.1 (45)	Buffalo	39	2302	13	203.5	-8
2345	32.9 (64)	Freedom	52	2332	13	196.8	-11.2

Table 2. Measured wind gusts (knots) for the 24 May 2011 Hampton Roads downburst event. Time is in UTC. WeatherFlow stations are identified by "WF".

Time	Gust Speed ms^{-1} (kt)	Location
2015	27.3 (53)	Poquoson (WF)
2017	29.3 (57)	Monitor-Merrimack Memorial Bridge Tunnel (WF)
2018	32.4 (63)	Willoughby Degaussing Station (PORTS)
2020	30.4 (59)	Hampton Flats (WF)
2036	34.5 (67)	1st Island (PORTS)
2040	31.9 (62)	3rd Island (WF)

Table 3. Measured wind gusts (knots) for the 25 August 2011 Chesapeake Bay downburst event. Time is in UTC.

Time	Gust Speed ms^{-1} (kt)	Location
2123	22.4 (44)	Potomac River Buoy (Intellicheck Mobilisa)
2212	24.1 (47)	Solomons Island (PORTS)
2224	19.9 (39)	Piney Point (PORTS)
2230	18.9 (37)	Cove Point (PORTS)

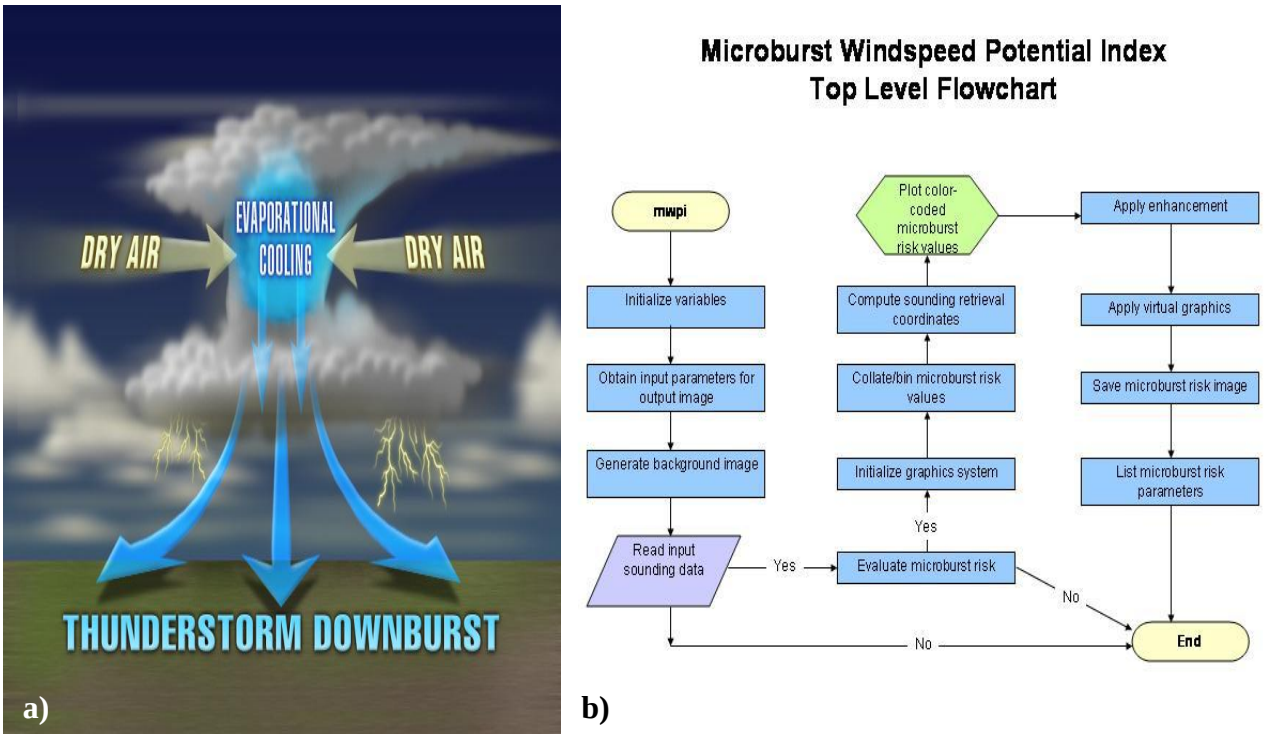

Figure 1. a) Graphical description of the physical process of downburst generation and b) flowchart illustrating the operation of the MWPI program in the McIDAS-X environment.

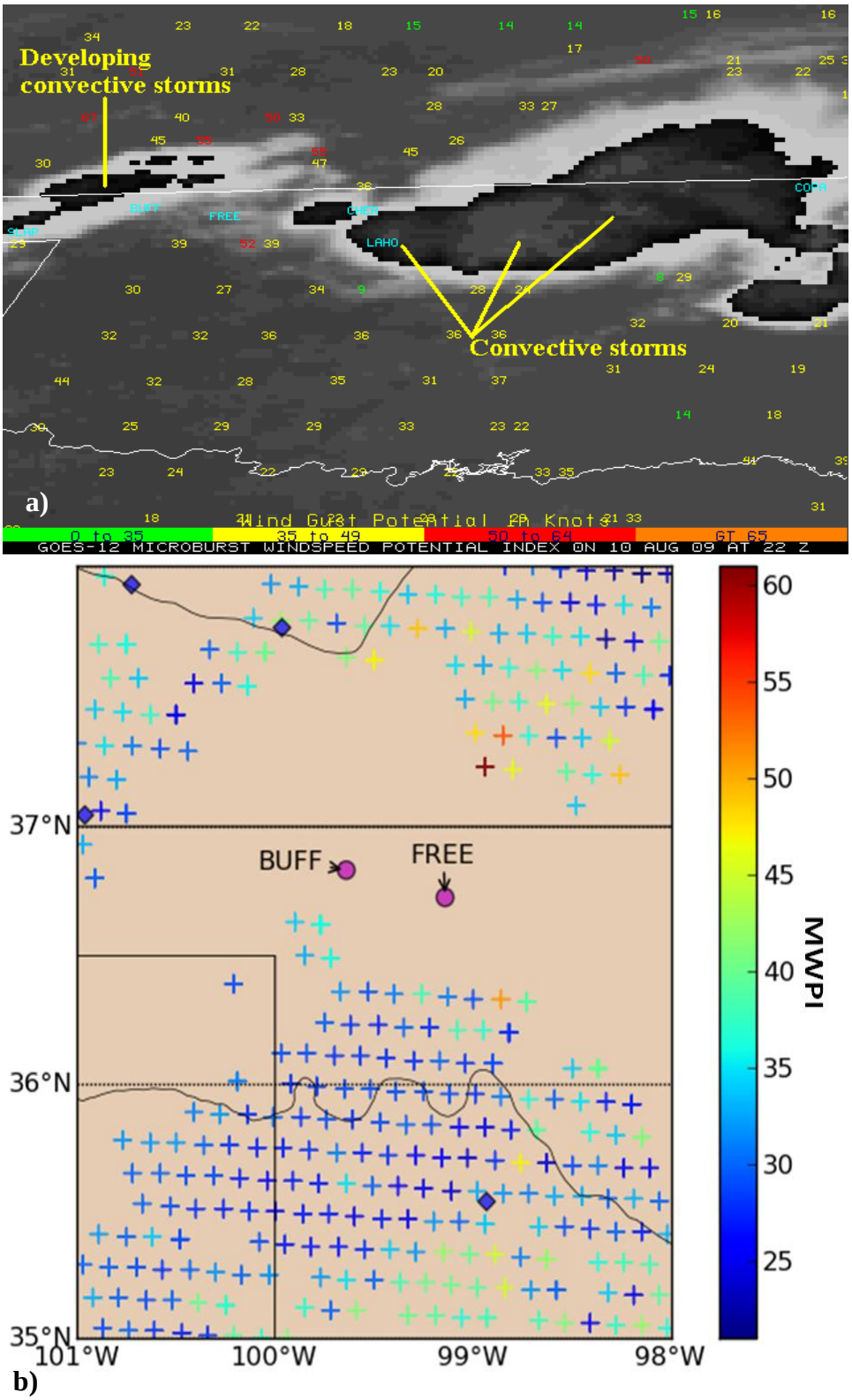

Figure 2. Comparison of GOES MWPI product visualizations on 10 August 2009 at 2200 UTC: a) McIDAS-X with MWPI values overlying enhanced infrared imagery and b) Graphyte. Four-letter identifiers of Oklahoma Mesonet stations listed in Table 1 are plotted over the images.

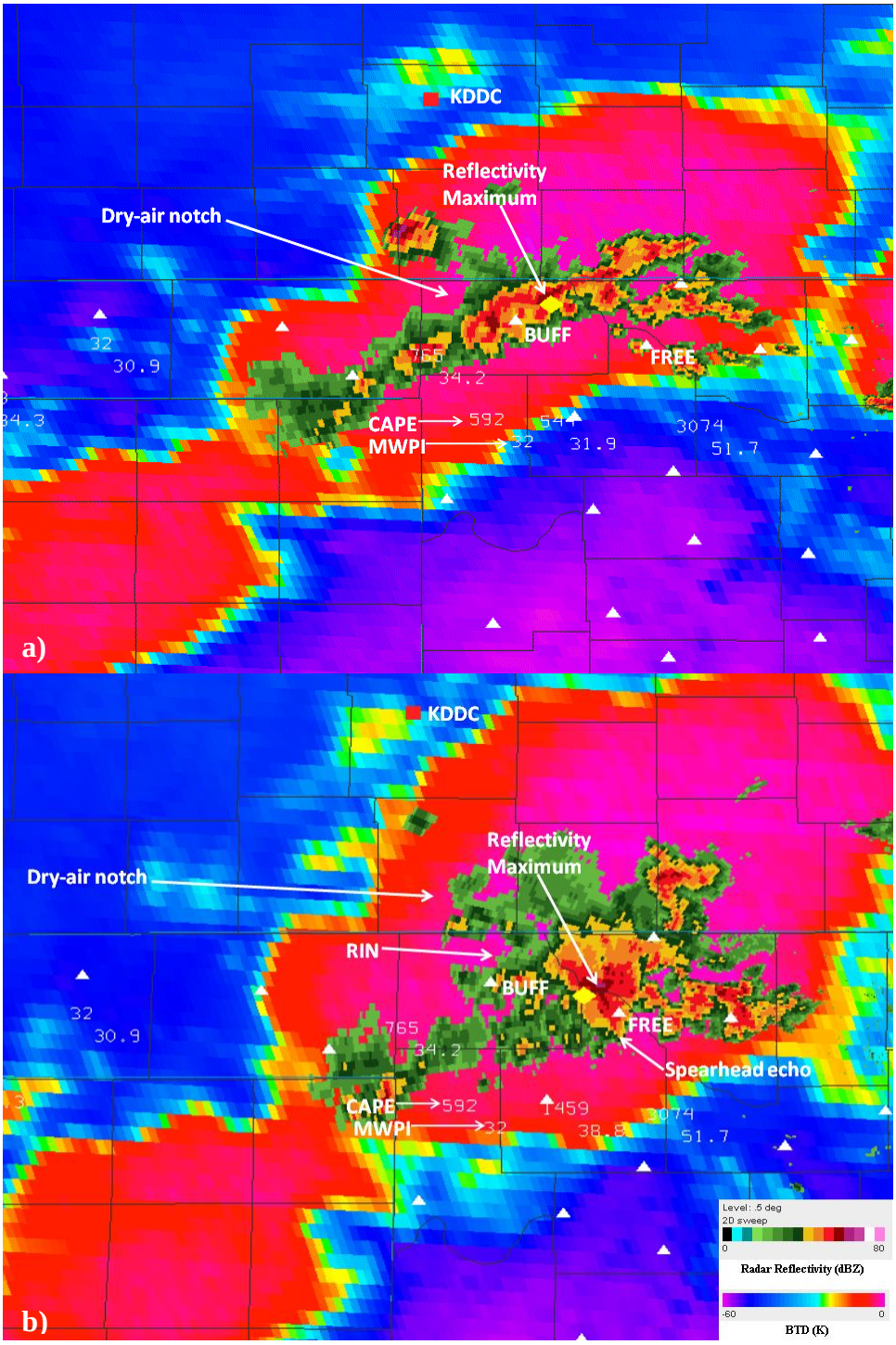

Figure 3. a) Composite image of GOES MWPI at 2200 UTC, GOES channel 3-4 BTD at 2302 UTC, and radar reflectivity from Vance AFB NEXRAD at 2305 UTC 10 August 2009; b) Composite image of GOES MWPI at 2200 UTC, GOES channel 3-4 BTD at 2332 UTC, and radar reflectivity from Vance AFB NEXRAD at 2343 UTC 10 August 2009. The overshooting top, as indicated by the Bedka algorithm, is marked with a yellow triangle. The location of the Dodge City RAOB is marked with a red square.

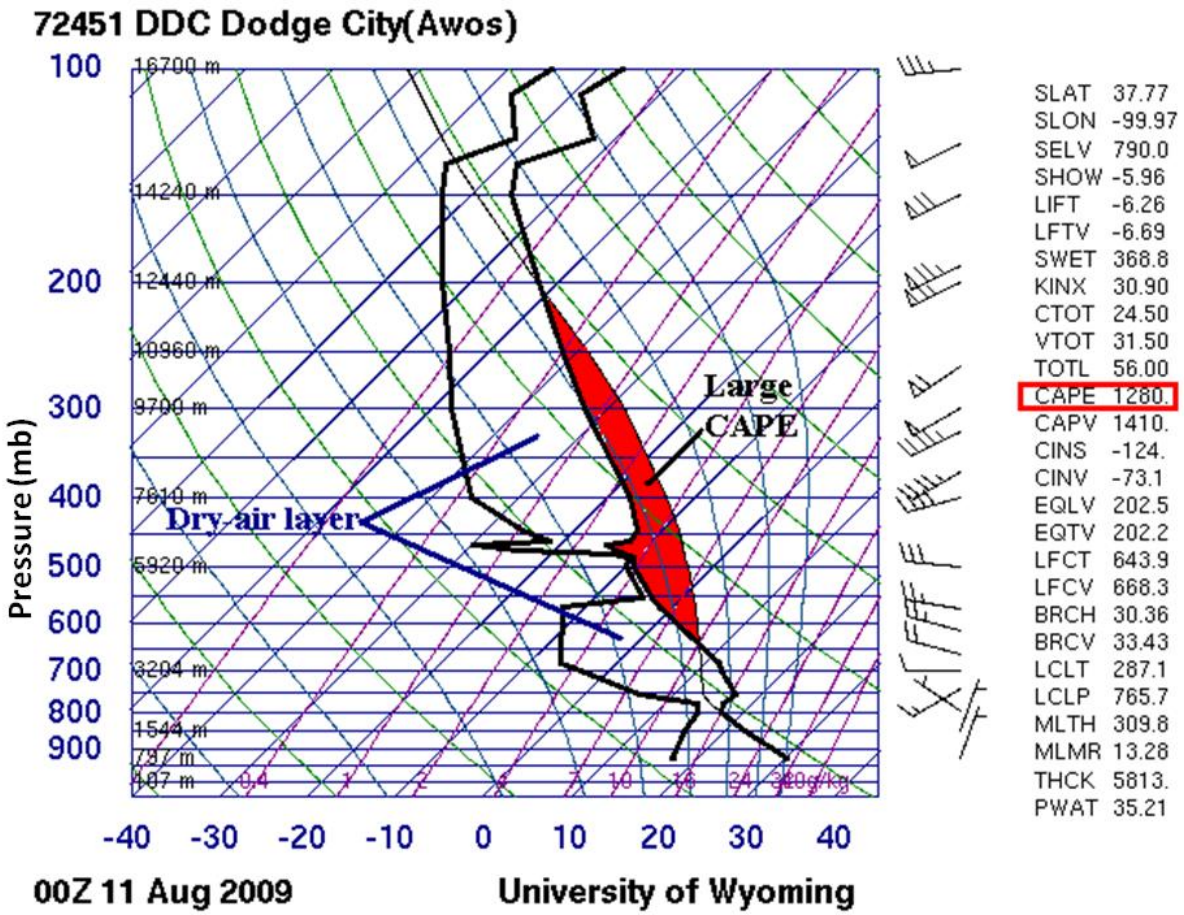

Figure 4. Dodge City, Kansas (DDC) radiosonde observation (RAOB) at 0000 UTC 11 August 2009. Courtesy of University of Wyoming.

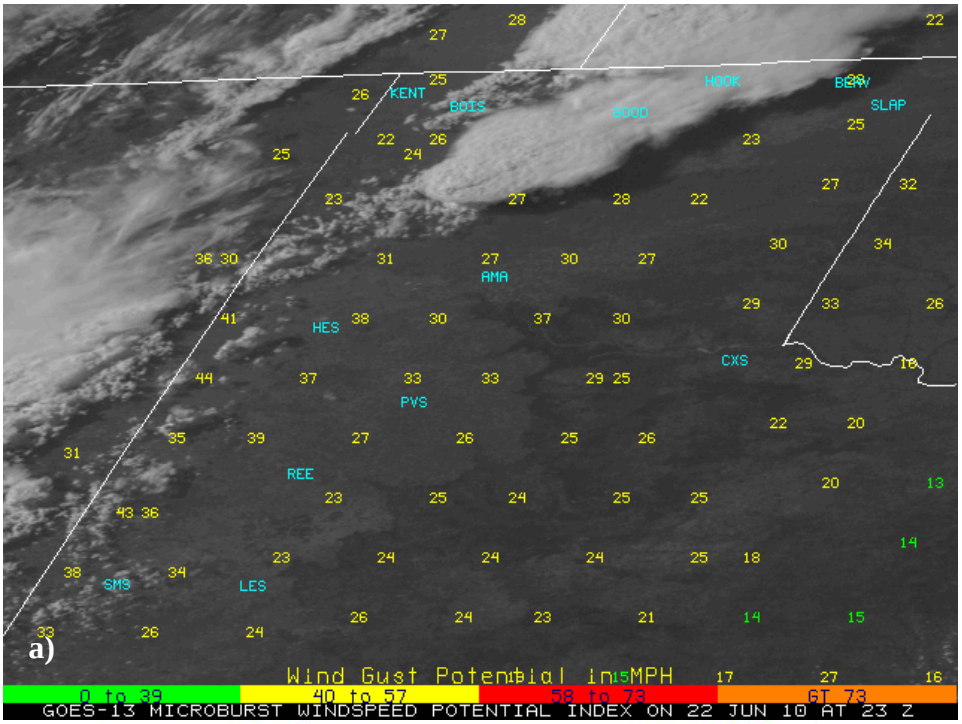

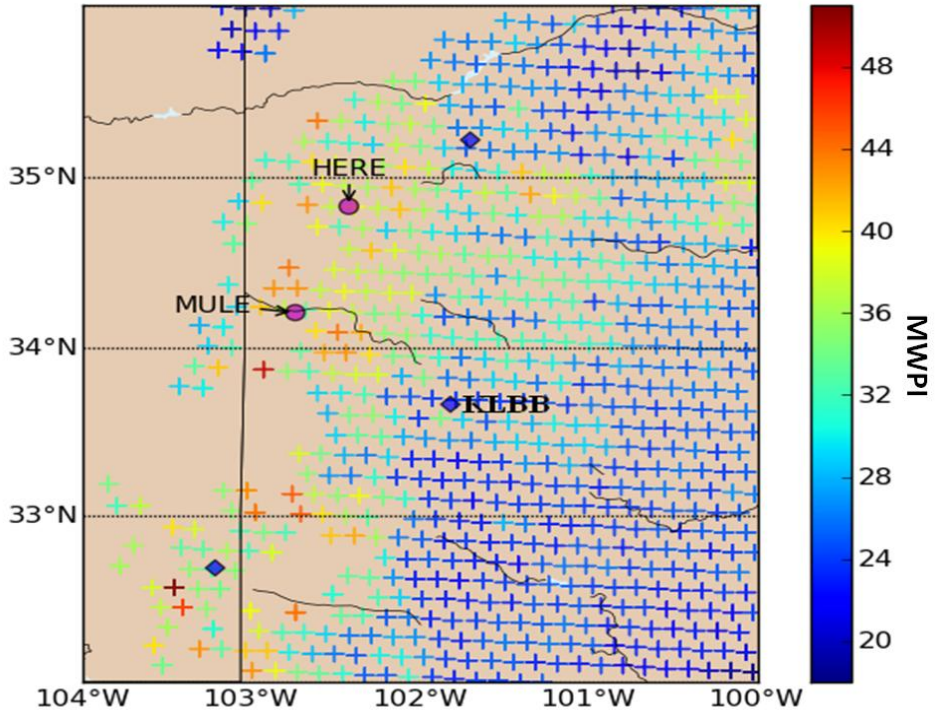

Figure 5. Comparison of GOES MWPI product visualizations on 22 June 2010 at 2300 UTC: a) McIDAS-X with MWPI values overlying visible imagery and b) Graphyte. Identifiers of West Texas Mesonet stations are plotted over the images.

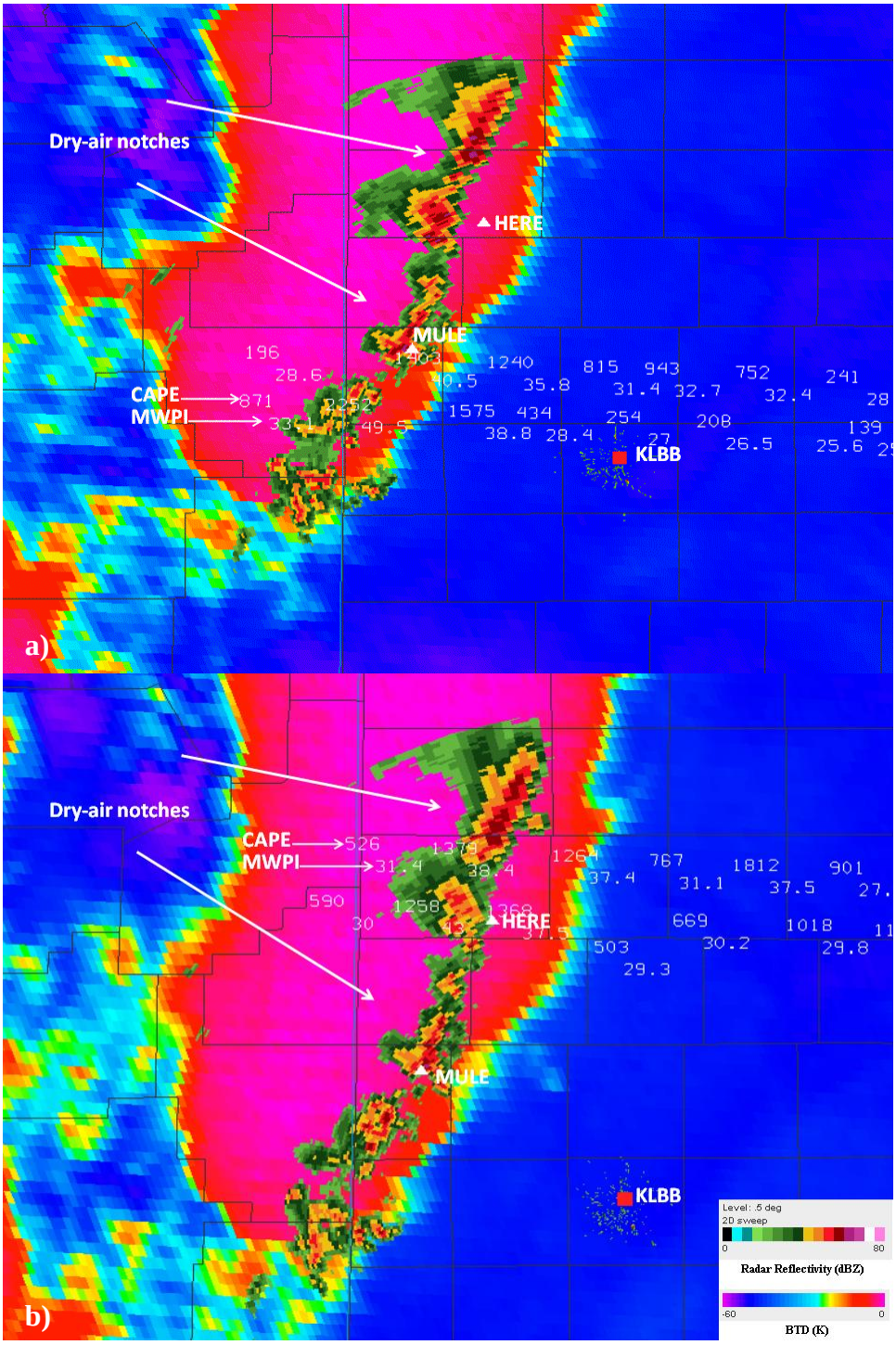

Figure 6. a) Composite image of GOES MWPI at 2302 UTC 22 June 2010, GOES channel 3-4 BTD at 0110 UTC, and radar reflectivity from Lubbock, Texas NEXRAD (KLBB) at 0115 UTC 23 June 2010; b) Composite image of GOES MWPI at 2302 UTC 22 June 2010, GOES channel 3-4 BTD at 0125 UTC, and radar reflectivity from Lubbock, Texas NEXRAD (KLBB) at 0124 UTC 23 June 2010. The location of the Lubbock GOES sounding is marked with a red square.

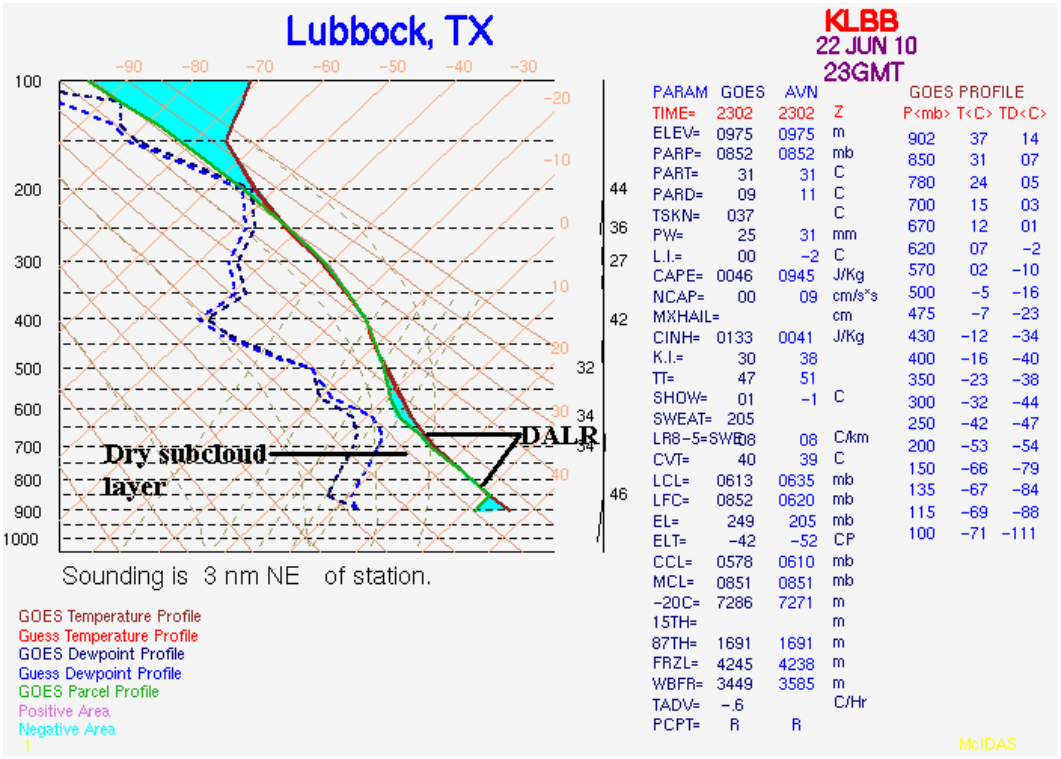

Figure 7. GOES sounding profile from Lubbock, Texas at 2300 UTC 22 June 2010.

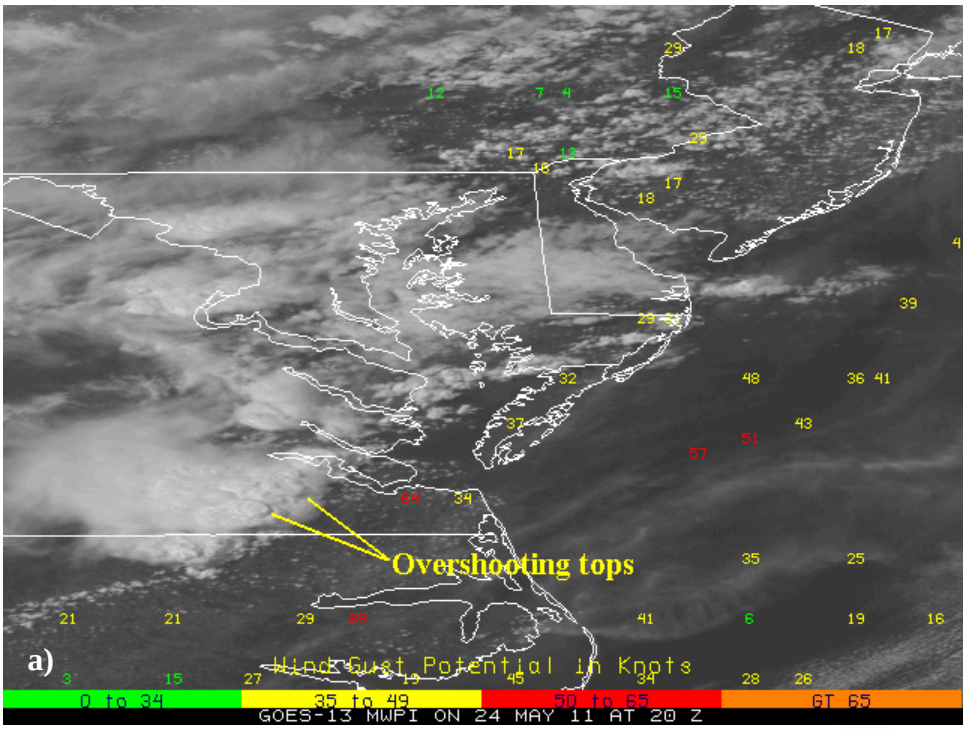

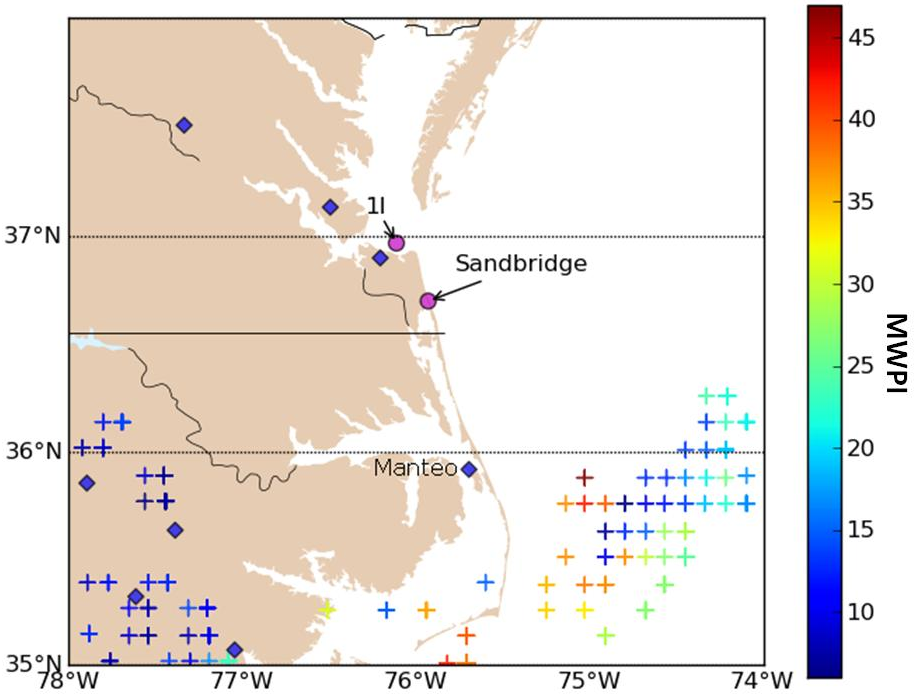

Figure 8. Comparison of GOES MWPI product visualizations on 24 May 2011 at 2000 UTC: a) McIDAS-X with MWPI values overlying visible imagery and b) Graphyte.

a)

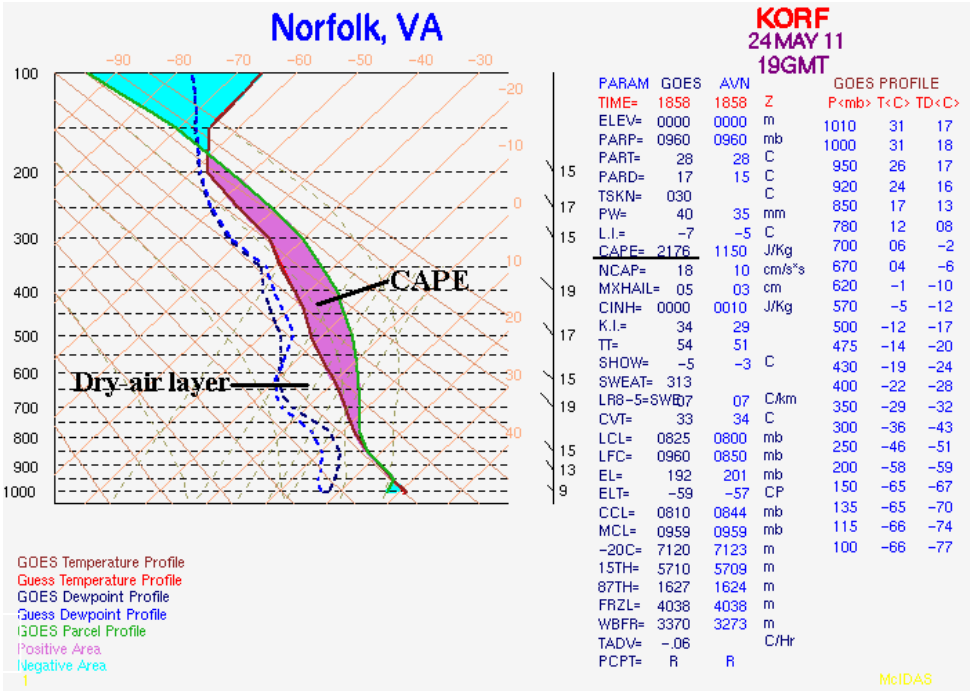

PARAM	GOES	AVN		GOES PROFILE P<mb>	T<C>	TD<C>
TIME=	1858	1858	Z	1010	31	17
ELEV=	0000	0000	m	1000	31	18
PARP=	0960	0960	mb	950	26	17
PART=	28	28	C	920	24	16
PARD=	17	15	C	850	17	13
TSKN=	030		C	780	12	08
PW=	40	35	mm	700	06	-2
L.I.=	-7	-5	C	670	04	-6
CAPE=	2176	1150	J/Kg	620	-1	-10
NCAP=	18	10	cm/s*s	570	-5	-12
MXHAIL=	05	03	cm	500	-12	-17
CINH=	0000	0010	J/Kg	475	-14	-20
K.I.=	34	29		430	-19	-24
TT=	54	51		400	-22	-28
SHOW=	-5	-3	C	350	-29	-32
SWEAT=	313			300	-36	-43
LR8-5=SWE	07	07	C/km	250	-46	-51
CVT=	33	34	C	200	-58	-59
LCL=	0825	0800	mb	150	-65	-67
LFC=	0960	0850	mb	135	-65	-70
EL=	192	201	mb	115	-66	-74
ELT=	-59	-57	CP	100	-66	-77
CCL=	0810	0844	mb			
MCL=	0959	0959	mb			
-20C=	7120	7123	m			
15TH=	5710	5709	m			
87TH=	1627	1624	m			
FRZL=	4038	4038	m			
WBFR=	3370	3273	m			
TADV=	-.06		C/Hr			
PCPT=	R	R				

b)

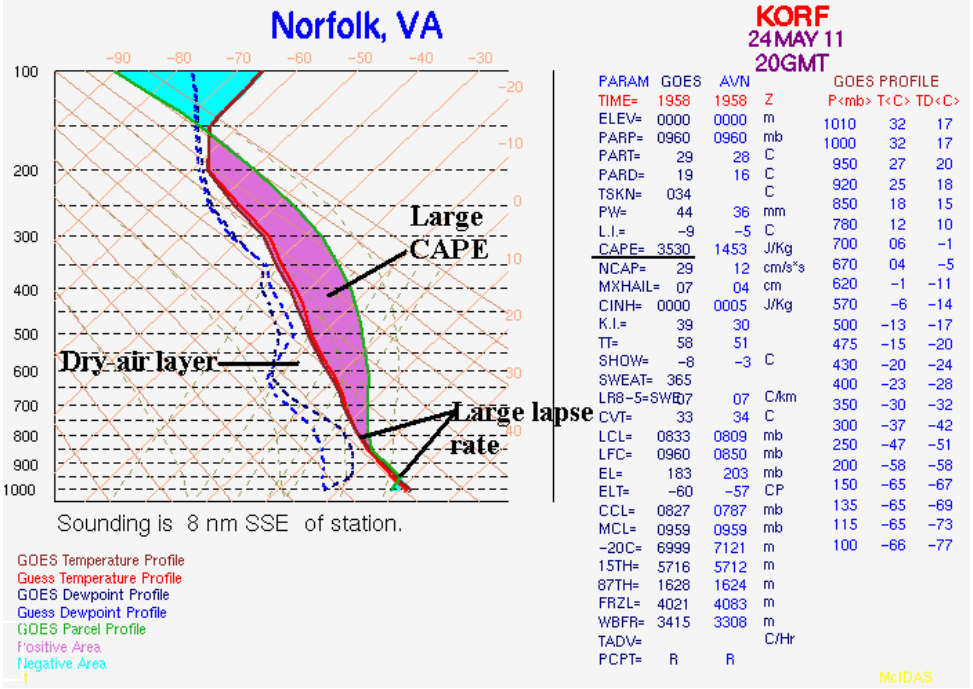

PARAM	GOES	AVN		GOES PROFILE P<mb>	T<C>	TD<C>
TIME=	1958	1958	Z	1010	32	17
ELEV=	0000	0000	m	1000	32	17
PARP=	0960	0960	mb	950	27	20
PART=	29	28	C	920	25	18
PARD=	19	16	C	850	18	15
TSKN=	034		C	780	12	10
PW=	44	36	mm	700	06	-1
L.I.=	-9	-5	C	670	04	-5
CAPE=	3530	1453	J/Kg	620	-1	-11
NCAP=	29	12	cm/s*s	570	-6	-14
MXHAIL=	07	04	cm	500	-13	-17
CINH=	0000	0005	J/Kg	475	-15	-20
K.I.=	39	30		430	-20	-24
TT=	58	51		400	-23	-28
SHOW=	-8	-3	C	350	-30	-32
SWEAT=	365			300	-37	-42
LR8-5=SWE	07	07	C/km	250	-47	-51
CVT=	33	34	C	200	-58	-58
LCL=	0833	0809	mb	150	-65	-67
LFC=	0960	0850	mb	135	-65	-69
EL=	183	203	mb	115	-65	-73
ELT=	-60	-57	CP	100	-66	-77
CCL=	0827	0787	mb			
MCL=	0959	0959	mb			
-20C=	6999	7121	m			
15TH=	5716	5712	m			
87TH=	1628	1624	m			
FRZL=	4021	4083	m			
WBFR=	3415	3308	m			
TADV=			C/Hr			
PCPT=	R	R				

Figure 9. GOES sounding profiles over Norfolk, Virginia at a) 1900 UTC and b) 2000 UTC 24 May 2011.

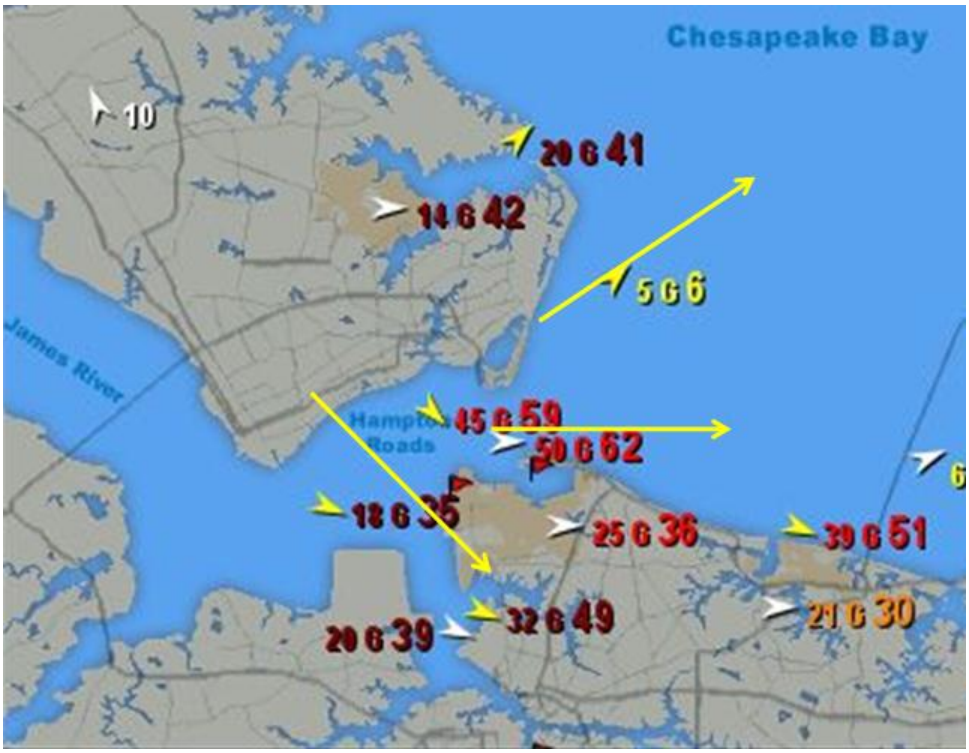

Figure 10. WeatherFlow surface observation plot at 2037 UTC 24 May 2011 showing the divergent nature of convective storm outflow winds over Hampton Roads area. Wind speeds are in knots. Yellow values represent wind gusts less than 20 knots, orange values represent wind gusts between 20 and 30 knots, dark red values indicate wind gusts between 30 and 50 knots, and red values indicate wind gusts greater than 50 knots. Courtesy Weatherflow Datascope.

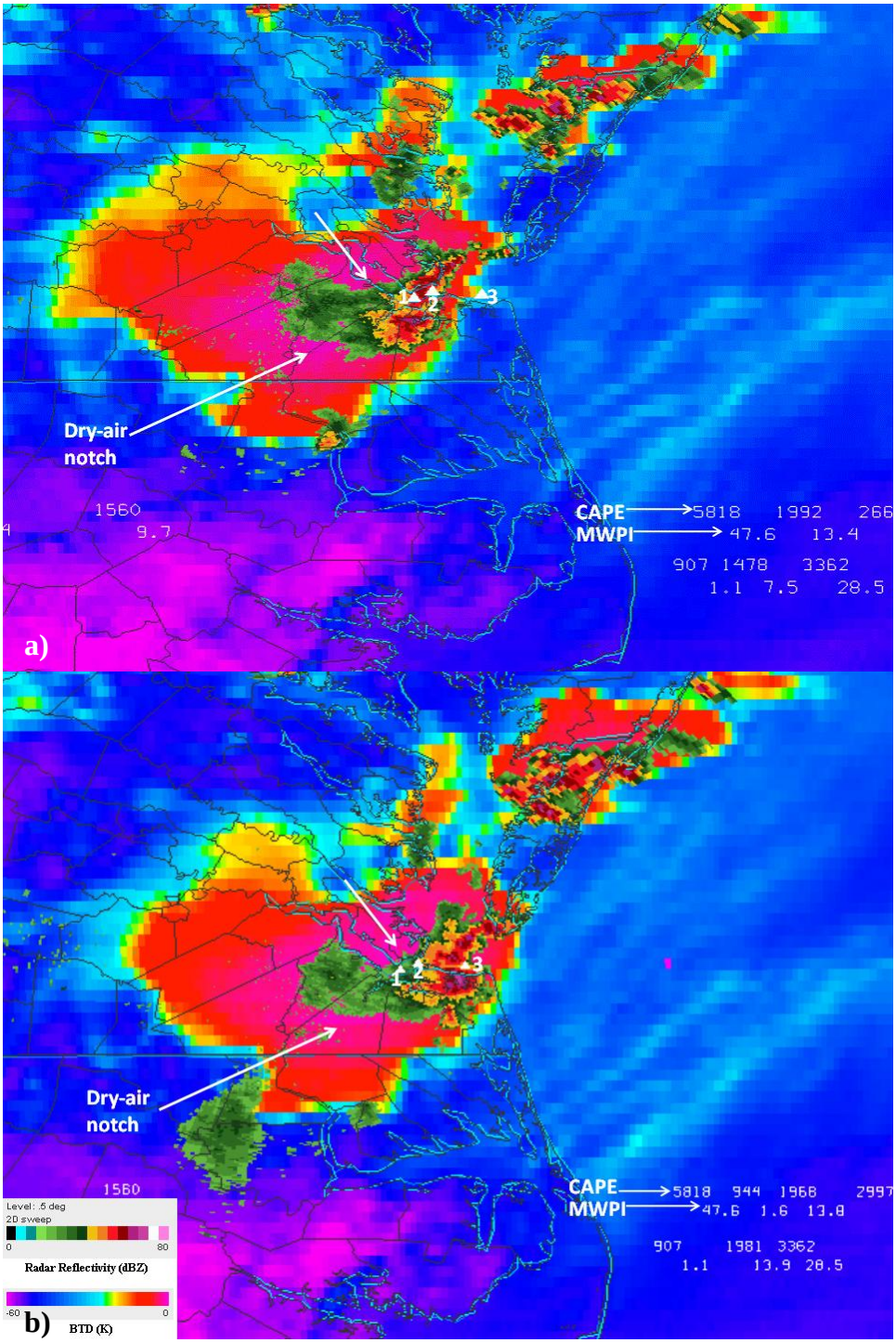

Figure 11. a) Composite image of GOES MWPI at 2000 UTC , GOES channel 3-4 BTD at 2025 UTC, and radar reflectivity from Wakefield, Virginia NEXRAD at 2025 UTC 24 May 2011; b) Composite image of GOES MWPI at 2000 UTC, GOES channel 3-4 BTD at 2040 UTC, and radar reflectivity from Wakefield, Virginia NEXRAD at 2039 UTC 24 May 2011. Triangular markers indicate the location of 1) Monitor-Merrimac Memorial Bridge-Tunnel, 2) Willoughby Degaussing Station, and 3) Chesapeake Bay Bridge-Tunnel observing stations, respectively.

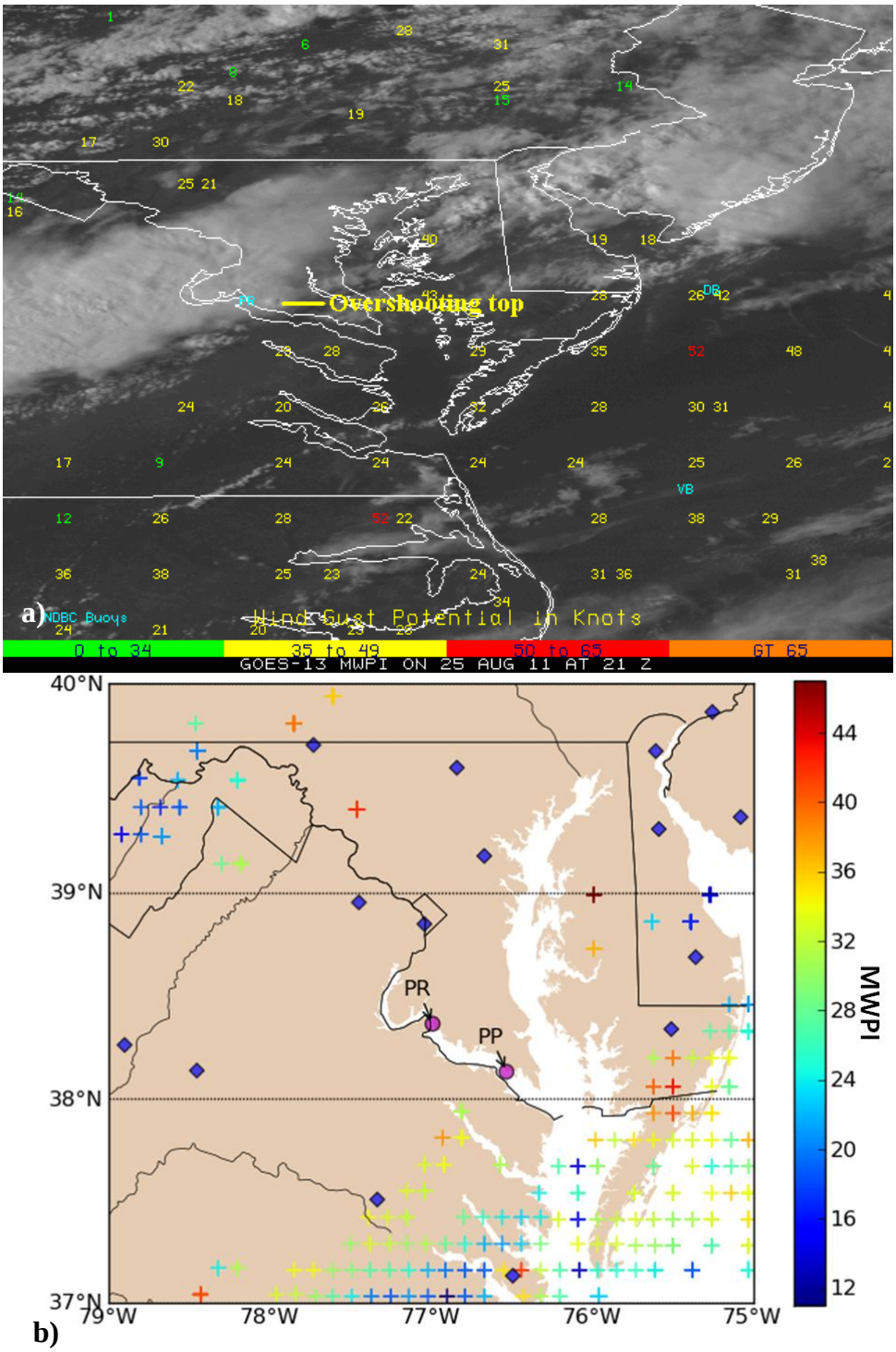

Figure 12. GOES MWPI products, with index values overlying visible imagery, at a) 2000 UTC and b) 2100 UTC 25 August 2011. "PR" marks the location of the Potomac River buoy and "PP" marks the location of Piney Point PORTS station.

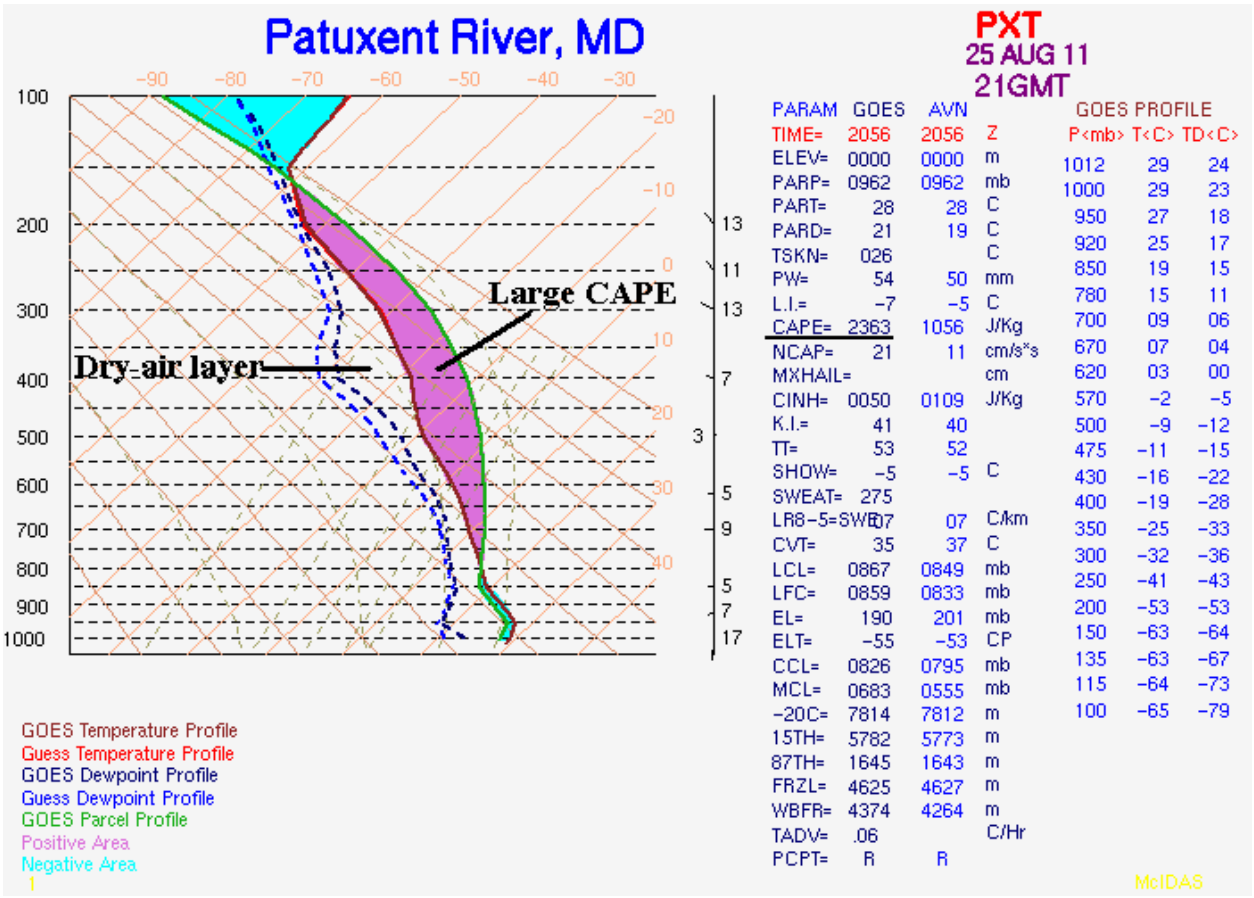

Figure 13. GOES sounding profile over Patuxent River, Maryland at 2100 UTC 25 August 2011.

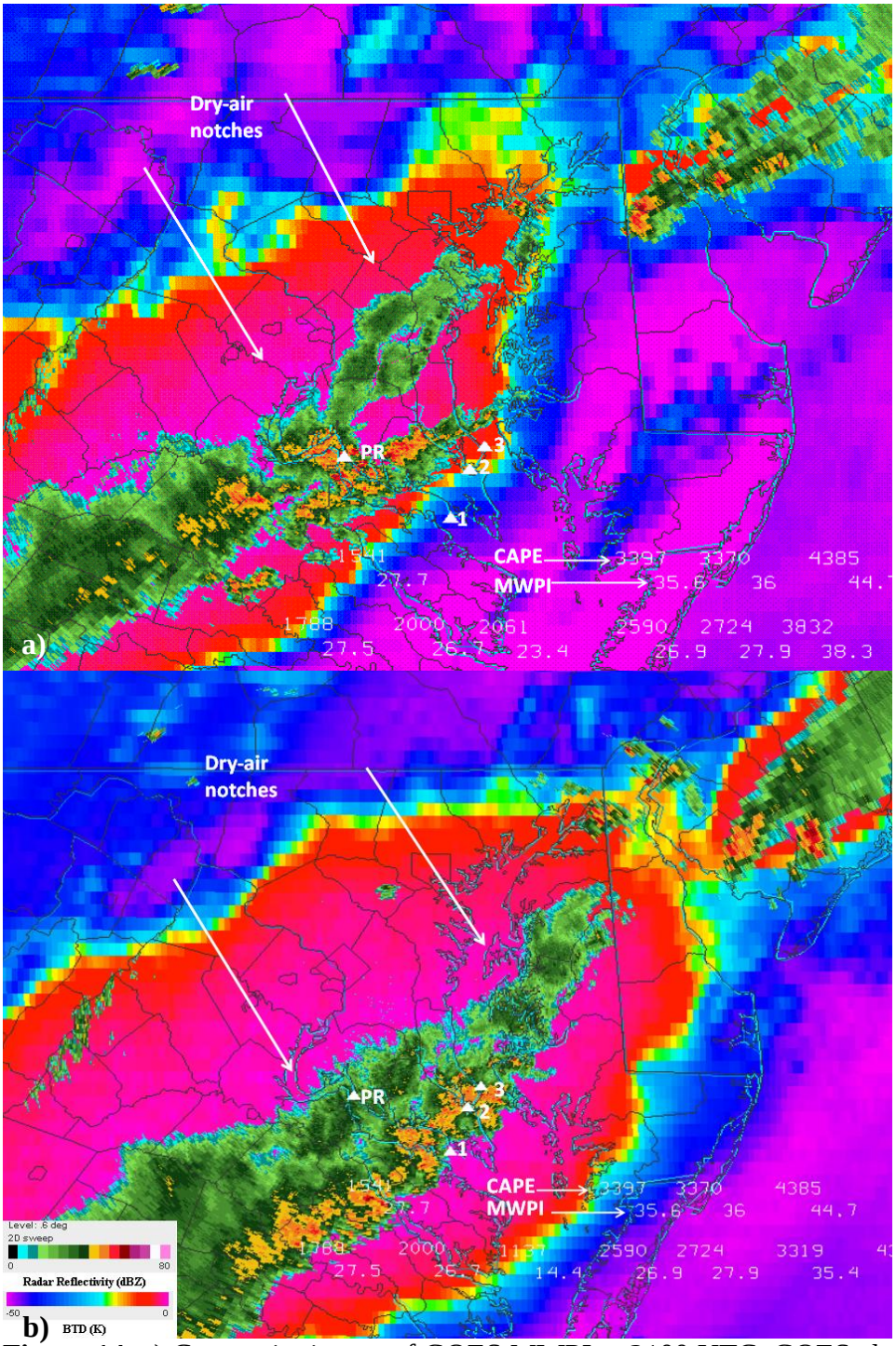

Figure 14. a) Composite image of GOES MWPI at 2100 UTC, GOES channel 3-4 BTD at 2115 UTC, and radar reflectivity from Andrews Air Force Base Terminal Doppler Weather Radar (TDWR) at 2121 UTC 25 August 2011; b) Composite image of GOES MWPI at 2100 UTC, GOES channel 3-4 BTD at 2215 UTC, and radar reflectivity from Andrews Air Force Base TDWR at 2227 UTC 25 August 2011. Triangular markers indicate the location of 1) Piney Point, 2) Solomons Island, and 3) Cove Point PORTS stations, respectively.

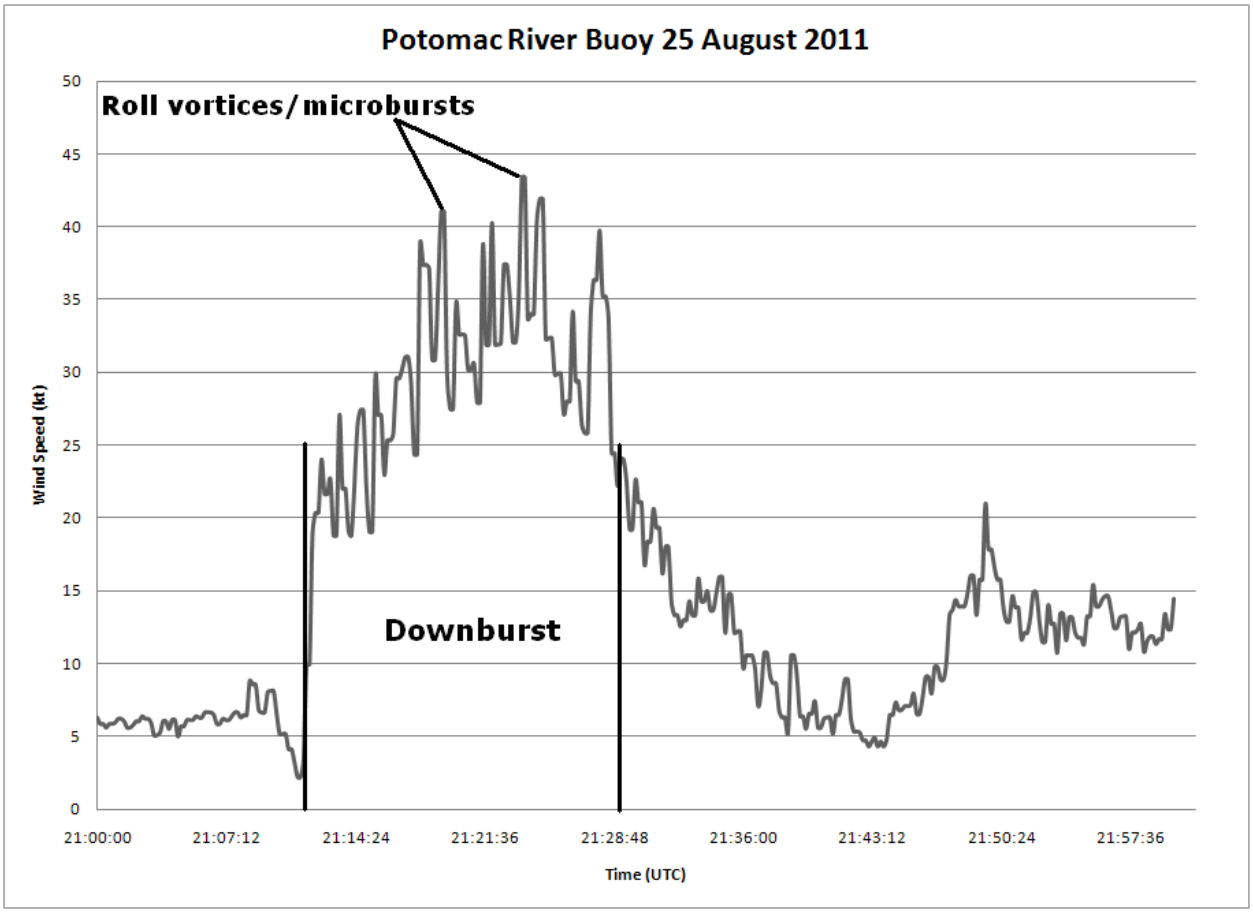

Figure 15. 25 August 2011 wind histogram from the Potomac River ("PR") buoy shows several peaks in wind speed, recorded by an acoustic wind sensor between 2110 and 2130 UTC, that likely indicate the passage of roll vortices and microbursts embedded within the larger scale downburst wind flow. Data courtesy of Intellicheck Mobilisa.

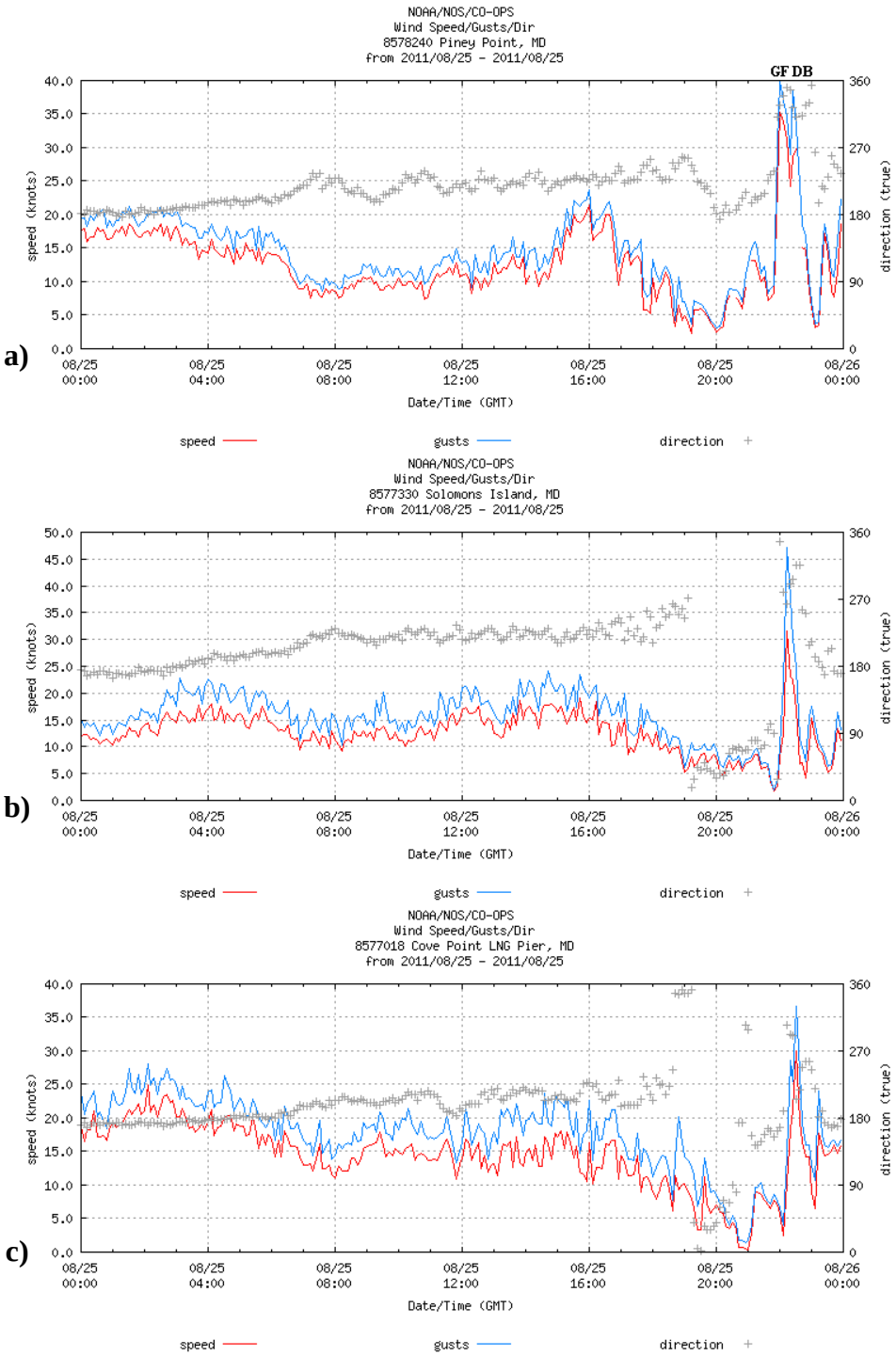

Figure 16. 25 August 2011 wind histograms from a) Piney Point, b) Solomons Island, and c) Cove Point PORTS stations that show downburst occurrence as a single peak in wind speed between 2200 and 2300 UTC. "GF" and "DB" mark the times of gust front passage and downburst occurrence at Piney Point.

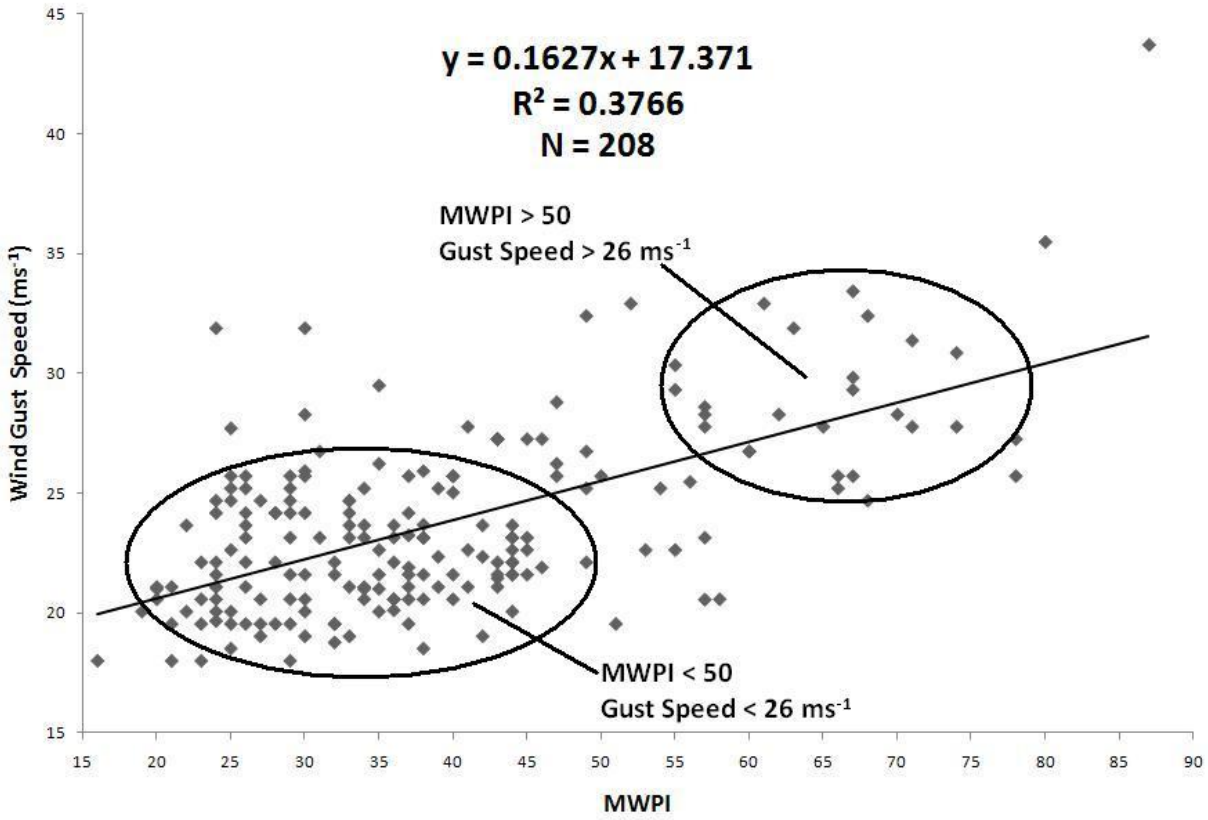

Figure 17. Statistical analysis of validation data over the Oklahoma and western Texas domain between June and September 2007 through 2010: Scatterplot of MWPI values vs. measured convective wind gusts for 208 downburst events.

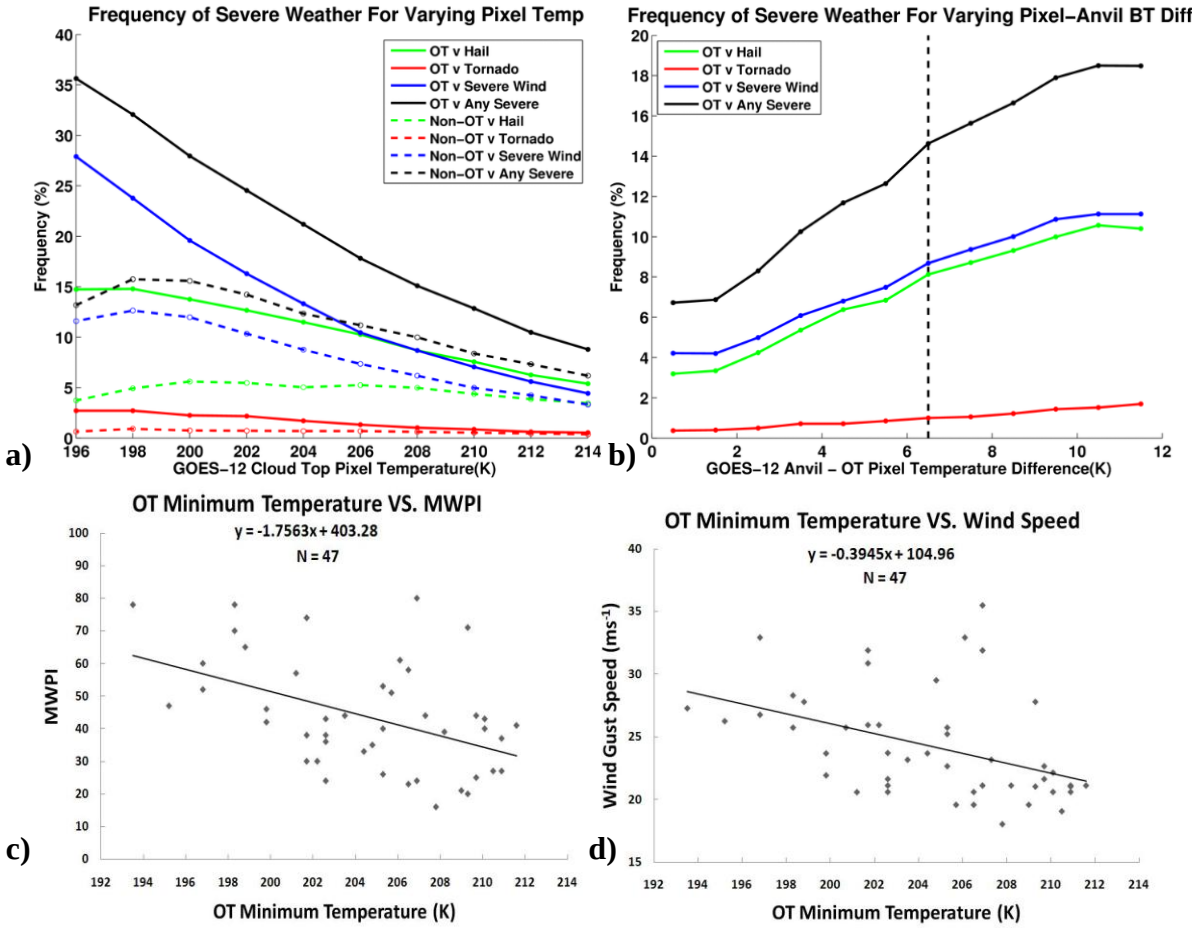

Figure 18. a) The frequency of severe weather for OTs (solid lines) and non-OT cold pixels (dashed lines) with varying IRW BT for each of the severe weather categories during the 2004-2009 warm seasons. b) Frequency of severe weather with varying BT difference between a pixel and the mean surrounding anvil temperature for each of the severe weather categories. The dashed line delineates the 6.5 °K criteria required for a pixel to be considered an OT. c) Comparison of scatterplots of convective OT minimum BT vs. GOES MWPI values and d) OT minimum BT vs. measured downburst wind gust speed (bottom) for 47 cases that occurred between 2007 and 2009.